國立臺灣大學理學院物理學研究所

碩士論文

Department of Physics

College of Science

National Taiwan University

Master Thesis

熱驅動之類神經網路元件及在 Cr_2O_3 中電性偵測反鐵磁性

Neuromorphic computing devices based on the asymmetric temperature gradient and the electrical detection of antiferromagnetism in Cr_2O_3

陳信儒

Hsin-Ju Chen

指導教授：黃斯衍 博士

Advisor：Ssu-Yen Huang, Ph.D.

中華民國 112 年 7 月

July, 2023

doi:10.6342/NTU202301357

doi:10.6342/NTU202301357

國立臺灣大學碩士學位論文
口試委員會審定書
MASTER'S THESIS ACCEPTANCE CERTIFICATE
NATIONAL TAIWAN UNIVERSITY

（論文中文題目）(Chinese title of Master's thesis)

非對稱溫度梯度驅動之類神經網路及在 Cr_2O_3 中電性偵測反鐵磁性

（論文英文題目）(English title of Master's thesis)

Neuromorphic computing devices based on the asymmetric temperature gradient and the electrical detection of antiferromagnetism in Cr_2O_3.

本論文係___陳信儒___(姓名)_R10222003_（學號）在國立臺灣大學_____物理所___(系/所/學位學程)完成之碩士學位論文，於民國_112_年_6_月_28_日承下列考試委員審查通過及口試及格，特此證明。

The undersigned, appointed by the Department / Institute of Physics_____ on _28_(date)_6_(month)_2023_(year) have examined a Master's thesis entitled above presented by___Hsin-Ju Chen____(name)_____R10222003_____(student ID) candidate and hereby certify that it is worthy of acceptance.

口試委員 Oral examination committee:

_____ _____ _____

（指導教授 Advisor）

_____ _____ _____

_____ _____ _____

系主任/所長 Director: _____

doi:10.6342/NTU202301357

Acknowledgement

碩士兩年說長不長說短不短，這兩年過得相當充實，學習到很多知識但也覺得還有很多東西學的不夠紮實；台大碩士班的教學相當紮實，在這強大的壓力底下也讓我搞懂很多在大學期間沒弄懂的物理，使我的基礎物理能力又更上一層樓。碩一期間，老師也鼓勵我們擔任助教工作，助教期間相當感謝許長仁講師的教導，在擔任助教期間，不僅有學習到基礎實驗技巧，也在指導學生的過程中，達到教學相長的功效。

在碩士這兩年期間，我非常感謝黃斯衍教授和曲丹茹老師的指導。從基本物理的指導到對研究態度的指引，都有相當嚴謹和邏輯的連貫性；老師總是強調必須知道為何做這個題目及所做的實驗意義為何，也要隨時保持批判性的思維來看待論文和研究成果。老師也時常鼓勵我們要多看論文，累積最新研究資訊並和老師討論，腦力激盪出新的想法，不能只當一個聽指令行事的技術員。在實驗上，老師也給學生很高的自由度，只要學生提出符合邏輯的點子，老師都相當支持學生往前走。在簡報技巧上，老師相當有一套，非常注重細節而且實事求是，協助我一頁一頁投影片修改，一句一句講稿仔細調整，使我能夠使用簡潔又吸引人的演說吸引台下的目光；也感謝老師支持學生投稿並參加會議，讓學生累積報告經驗並與全世界的物理學家進行交流討論；老師說過”人”才是有價值的資產，在這樣的氛圍底下學習，學生才能無止盡的成長。

能夠有現在的研究成果，真的要感謝黃斯衍老師和曲丹茹老師的指導；也很感謝

doi:10.6342/NTU202301357

同期在實驗室的同仁(智傑學長、彥璋學長、柏勳學長、顏慶助理、冠舟助理、康國、俊維學弟、淳芸學妹、家晞學妹、裕鈞學弟、哲宇學弟)在實驗上的協助，也希望後來加入的同仁(首睿學長、文淵學長、郁升、立信、晉德、宏杰助理、欣蔓助理、哲宇學弟、晉佑學弟、昭瑋學弟、軒誠學弟)，大家在未來的道路上能一切順利。

最後感謝在背後默默支持我的家人(爸爸、媽媽)及朋友們，有你們的支持，我才能在低潮時持續向前進，完成碩士學歷，謝謝你們。

陳信儒 謹誌

doi:10.6342/NTU202301357

中文摘要

為了解決傳統計算機架構:馮諾依曼架構(Von Neumann architecture)中的高能耗問題，基於反鐵磁（AFM）的自旋電子學被認為是有前途的候選者。與現今發展的鐵磁性自旋電子學相比，反鐵磁材料被認為會是下一主要的發展方向，其主要優點是不存在雜散場並且不會受到外部磁場所擾動。另一方面，受人腦啟發的全新架構也是未來應用的另一個重要方向。人腦神經網絡的低功耗和高效能是研究的主要動機。模擬人腦神經網絡的電子元件架構對於實現信息處理和決策的人工智能至關重要。在過去的幾十年裡，不同類型的類神經網路元件已經被開發出來，例如由離子擴散引起的憶阻器、由電壓閾值切換的結構相變元件(漸進結晶/非晶化)，以及基於磁區切換自旋電子學的器件。然而，這些設備也各自面臨挑戰，包括積體電路的可擴展性以及權重變化的非線性。因此，本篇論文提出替代方法來解決上述挑戰。在本研究中，我們介紹了一種基於非對稱溫度梯度的多層多腳位類神經網路元件；我們的元件展示出廣泛的突觸功能，包括突觸權重的增強、抑制以及反對稱和對稱脈衝時序依賴可塑性（STDP）。此熱驅動之類神經網路元件為未來人工智能的硬體實現提供了一個平台。

另一方面，我們嘗試利用自旋翻轉(Spin-flop)來實現尼爾矢量(Néel vector)翻轉。利用電性量測來檢測和操縱尼爾矢量已經在塊狀單軸的反鐵磁材料 Cr_2O_3 中實現。在這篇論文中，我們嘗試在 Al_2O_3 基板上生長高品質的單晶 Cr_2O_3 薄膜，並嘗試用電性量測方法檢測自旋翻轉。這些工作使我們向下一代自旋電子學邁出了

doi:10.6342/NTU202301357

一步。

關鍵字: 多層多腳位類神經網路元件、突觸可塑性、脈衝時序依賴可塑性、非對稱溫度梯度、自旋電子學、異常霍爾效應、電性偵測反鐵磁性

doi:10.6342/NTU202301357

Abstract

To deal with the high energy consumption problem in the conventional computer architecture (Von Neumann architecture), antiferromagnetic (AFM) based spintronics is regarded as the promising candidate. The absence of a stray field and the robustness against external magnetic perturbation are the main advantages for antiferromagnetic materials compared with ferromagnetic-based spintronics. On the other hand, a brand-new architecture inspired by the human brain is another crucial platform for future application. The low power consumption and high performance the biological neural network enjoys are the primary motivations for neuromorphic computing devices. Neuromorphic computing devices, which emulate biological neural networks, are crucial in realizing artificial intelligence for information processing and decision-making. In the past decades, different types of neuromorphic computing devices with multiple resistance levels (defined as synaptic weight) have been developed, such as oxide-based memristors caused by ion diffusion, phase transition-based devices caused by threshold switching, progressive crystallization/amorphization, and spintronics-based devices caused by magnetic domain switching. However, these devices face significant challenges, including disruptions in the reading process, limited scalability in integrated circuits, and non-linearity in weight change. Therefore, alternative approaches are required to solve the above challenges. In this study, we introduce a

doi:10.6342/NTU202301357

multi-layer-multi-terminal neuromorphic computing device based on the asymmetric temperature gradient. Our device exhibits a wide range of synaptic functions, including potentiation, depression, and both anti-symmetric and symmetric spike-timing-dependent plasticity (STDP). The thermal driving strategy offers an energy-efficient platform for future neuromorphic computing devices to achieve artificial intelligence. On the other hand, we tried to employ the spin-flop transition to realize the AFM switching. The electrical detection and manipulation of the Néel vector have been realized in bulk uniaxial antiferromagnet Cr_2O_3. In this work, we also tried to grow high-quality epitaxial Cr_2O_3 thin film on Al_2O_3 substrate and tried to detect the spin-flop transition electrically. These works give us a step toward the next generation of electronics.

Keywords: multi-layer-multi-terminal neuromorphic computing devices, synaptic plasticity, spike-timing dependent plasticity, asymmetric temperature gradient, spintronics, anomalous Hall effect, electrically detection of antiferromagnetism.

doi:10.6342/NTU202301357

目錄

doi:10.6342/NTU202301357

doi:10.6342/NTU202301357

List of Figures

doi:10.6342/NTU202301357

doi:10.6342/NTU202301357

doi:10.6342/NTU202301357

doi:10.6342/NTU202301357

doi:10.6342/NTU202301357

Chapter 1 Introduction and literature review

The conventional computers are built based on the Von Neumann architecture which was proposed by John von Neumann in 1945 [1]. With the development of semiconductor industry and the design of very large-scale integrated circuits (VLSI), the Von Neumann architecture has achieved great success and brought human life with powerful computers and smart phones. However, as transistors continue to scale down, they tend to consume more power and become less stable. Therefore, due to the rapid development of information technology, there is a need for low power consumption and highly efficient calculation. Moreover, the Von Neumann architecture has a bottleneck due to the separated design of CPU and memory [2]. Nowadays, to solve these problems, physicists have been focusing on two ways. One is the Quantum computing which utilize the principles of quantum mechanics such as entanglement and superposition to perform complex calculation. The other one is neuromorphic computing which emulates the human brain to be the new computing architecture. In this work, we present a multi-layer-multi-terminal neuromorphic computing device based on asymmetric temperature gradient.

doi:10.6342/NTU202301357

1.1 Neuromorphic computing

Human brain can process information with highly parallel calculation and low power consumption (~20 W), which inspired us to build a new computing architecture emulating the biological neural network. Unlike the conventional computer which consumes energy in transmitting and storing information between the memory and the processor, biological neural network stores information locally where it is processed. Therefore, the hardware implementation of brain-inspired computing (neuromorphic computing) has become an attractive trend for future computing paradigm. In the past decades, people are working on electronically emulating synaptic functionalities such as the weight-potentiation, weight-depression and spike-timing dependent plasticity (STDP) [3]. However, the reported artificial synaptic devices face critical challenges in stability and scalability [3]. Therefore, an alternative approach to realize the neuromorphic computing devices with functionalities resembling synapses is demanded.

doi:10.6342/NTU202301357

1.1.1 Memristor-based neuromorphic computing device

The hardware implementation of neuromorphic computing devices requires special electronics having the similar properties with biological neural network. Namely, we need solid state circuits containing artificial neurons and artificial synapses to build the completed artificial neural network. For the artificial neurons, many groups are using CMOS circuits to realize the neuronal functionalities [4]. To emulate synaptic plasticity, the electronics need a tunable physical quantity which can be defined as the synaptic weight under external stimulation. Moreover, the variation of the synaptic weight must follow STDP. Recently, several types of artificial synapse were proposed including ion-migration based memristors, phase-change-based devices, and spintronics based devices. However, these devices still face a lot of challenges.

Memristors two-terminal circuit elements are wildly used in resistive random-access memory (RRAM) in modern electronics. Memristors are the metal-insulator-metal structure and the operations are read and write. The operations are sketched in Figure 1-1. The writing process contains two parts: the SET process and the RESET process. In the SET process, the positive voltage is applied on the memristors. Therefore, the resistance is changed from high resistance state to low resistance state. On the other

doi:10.6342/NTU202301357

hand, during the RESET process, the negative voltage is applied, and the resistance is changed from low resistance state to high resistance state. Additionally, the reading process is done by measuring the resistance of the device. The controllable resistance in memristor is defined as the synaptic weight. However, even though the resistance of memristors can be easily controlled by voltage, the variation of resistance is not linear. In addition, the reading process could cause interference since the writing and reading process shares the same terminal. Furthermore, the variation of the synaptic weight is non-linear which is common in memristor but not favorable for synaptic operation.

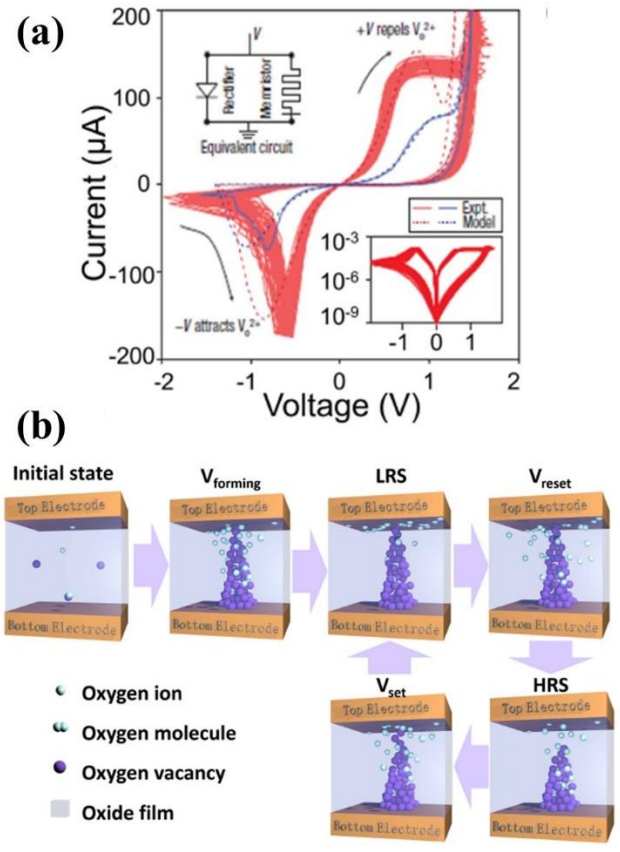

Figure 1-1: Operations of memristors. (a) Experimental data of I-V curve in memristor.

doi:10.6342/NTU202301357

(b) Schematic diagram of the switching in the anion migration based memristor. Revised from [3].

Beside emulating the ability to arbitrarily variate synaptic weight, the neuromorphic computing device is also required to emulate the spike-timing dependent plasticity (STDP). STDP is the most important function of synaptic plasticity which variates its synaptic weight based on the relative timing between the neurons received the spike. For example, Sung Hyun Jo *et al*. first demonstrated the anti-symmetric STDP in memristor by variating the pulse width of the writing gate voltage [4]. As shown in Figure 1-2 (a), by transfer the pulse width information into relative timing information, the anti-symmetric STDP was demonstrated. Comparing with the biological system (rat hippocampal) as presented in Figure 1-2 (b), the similar behavior can be obtained in memristor based system by varying pulse width.

doi:10.6342/NTU202301357

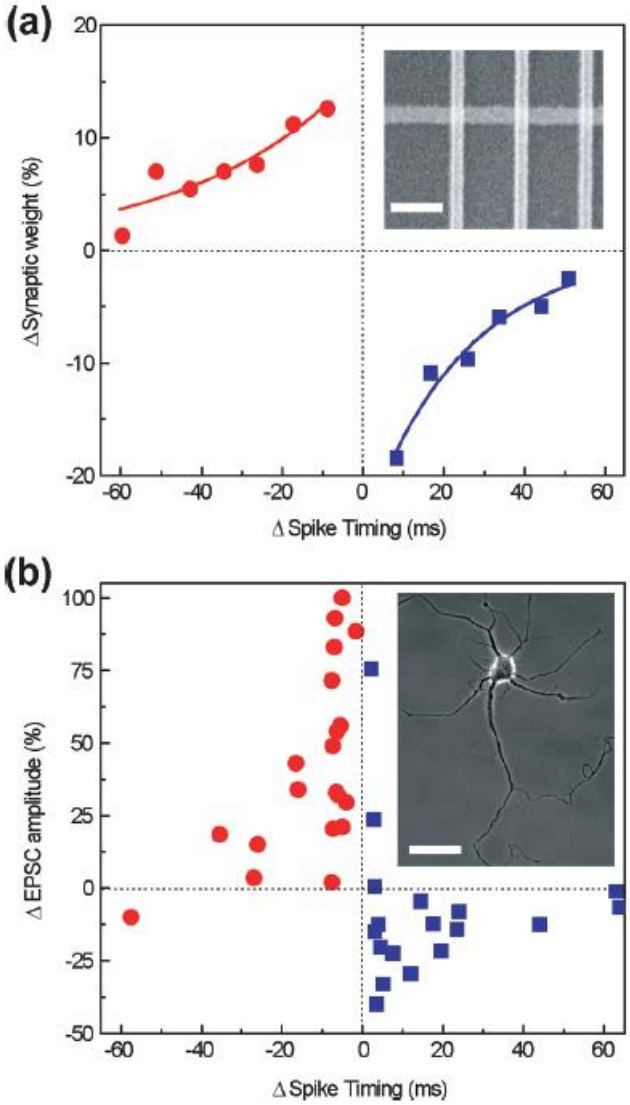

Figure 1-2: Demonstration of anti-symmetric STDP in memristor based neuromorphic computing device. (a) The variation of resistance in memristor (synaptic weight) verse the relative timing of the spikes. Revised form [4]. (b) The change in excitatory post-synaptic current measured in rat hippocampal neurons. Revised form [5].

1.1.2 Spintronics based neuromorphic computing device

Another neuromorphic computing devices are based on the magnetic materials.

doi:10.6342/NTU202301357

For example, the spin transfer torque magnetic memory (STT-MRAM) which changes the magnetization state without external magnetic field is a candidate of artificial synapses [3]. The STT-MRAM is consisted of many magnetic tunnel junctions (MTJ). The resistance of the MTJ can be controlled by the relative orientation of the magnetization of the two ferromagnetic layer. As shown in Figure 1-3 (a), the thicker ferromagnetic layer with perpendicular magnetization direction is defined as the pinned layer. The other ferromagnetic layer with thinner thickness is defined as the free layer whose magnetization direction can be variated by the injected spin current. By variating the magnetic domain configuration of the free layer, it can tune the resistance state between two resistance state: the highest resistance state of anti-parallel alignment of magnetic moment (free layer and pin layer) and the lowest resistance state of parallel alignment of magnetic moment [3]. The multi-level resistance can be achieved in multi domain configuration neither anti-parallel nor parallel. Therefore, the multi-level resistance state can be created and emulate the synaptic functionalities.

However, the ferromagnetic based spintronics suffer the influence of stray field when scaling down. The magnetic domains could reduce to a single domain in extremely small-scale devices, which preventing the formation of multi-level resistance state. Moreover, although the reading power consumption for MTJ based device is extremely low, the writing power consumption is much higher [3]. To change the magnetization

doi:10.6342/NTU202301357

direction of the free layer by injected spin current, it usually needs high power consumption (up to 100 fJ/spike), which is not suitable for future applications in neuromorphic computing.

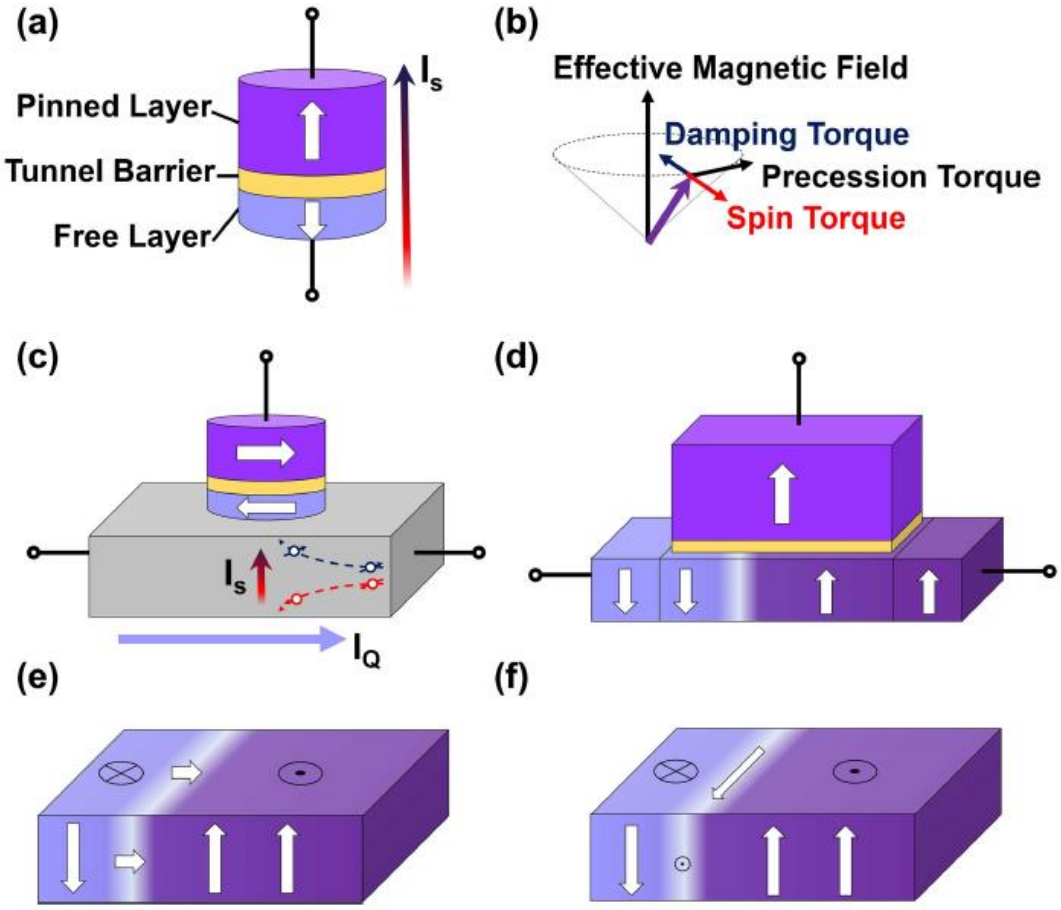

Figure 1-3: (a) Schematic spin transfer torque magnetic memory (STT-MRAM). (b) The dynamics of magnetization under the influence from the injected spin current. (c) Spin orbit torque from spin Hall effect through the heavy metal layer. (d) Schematics of domain wall motion device. € Néel vector and (f) Bloch domain walls observed in narrow and wider nanostrips with perpendicular magnetic anisotropy. Revised from [3].

doi:10.6342/NTU202301357

1.1.3 Phase-change mechanics based neuromorphic computing device

Another common mechanism for emulating neural network is the phase change mechanics (PCM) based devices. Like previous neuromorphic computing devices, the multi-level resistance state is also created. The structure of the materials used in phase-change mechanics based device can be tuned by external voltage. The variation between high resistance and low resistance state are based on the crystallization and amorphization processes [3]. For example, the Ge-Sb-Te (GST) ternary phase diagram is the most studied PCM system. Tuma *et al*. demonstrated that the basic neural operation based on PCM material $Ge_2Sb_2Te_5$ [6]. As shown in Figure 1-4 (a), the voltage pulse sequence was applied through bottom or top electrode. Once the current flows through the PCM materials, a part of area is heated up and gradually crystallized. Therefore, the amorphous area in the device shrinks due to the crystallization changing its resistance state. However, the PCM suffers a challenge due to the PCM itself. The crystallization and amorphization change the density of the PCM materials, which would be greatly harmful for the stability in integrated circuits [3]. The variation of the density inside the device might damage the device structure during operations.

doi:10.6342/NTU202301357

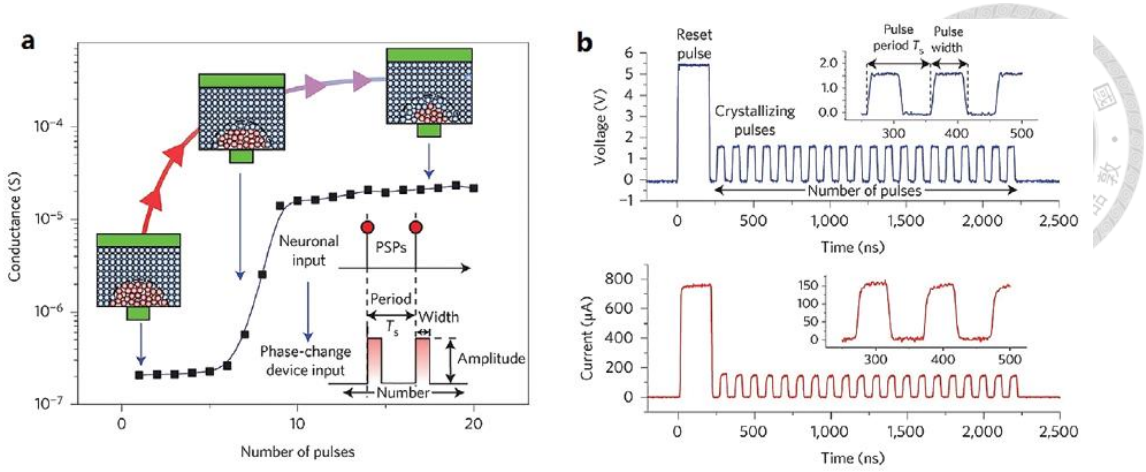

Figure 1-4: (a) The variation of conductance by the number of pulse voltage. The schematic inserts show the variation of amorphous area. (b) The voltage pulse sequence and the corresponding current used in operating the PCM device. Revised from [6].

To sum up, various types of artificial synaptic device have been realized. However, they all still suffer their own challenges such as non-linearity and the stability in future applications. Therefore, an alternative mechanism with stable operation and linear variation of synaptic weight is needed.

1.2 Antiferromagnetic switching

1.2.1 Eight-terminal device

Spintronics which manipulate the spin angular momentum by spin current have been developed to reduce power consumption and scale. During these years, the antiferromagnetic materials (AFM) have great potential in this regard due to its plenty of useful properties. For example, antiferromagnetic Néel vector is robust against

doi:10.6342/NTU202301357

magnetic perturbation and has ultrafast dynamics. Moreover, Néel vector has no stray field, allowing higher density of devices. In 2016, the electrical AFM switching was first demonstrated by P. Wadley *et al.* in CuMnAs with eight-terminal structure as shown in Figure 1-5 (a) [7]. They tried to use Néel-order Spin-orbit torque (NSOT) generated from inverse spin-galvanic effect to switch Néel vector. The resulting switching was observed as sawtooth signal in transverse resistance [see Figure 1-5 (b)]. After that, X. Z. Chen *et al*. also proposed the similar AFM switching in Pt/NiO heterostructure [8]. The sawtooth signal was also observed in the same eight-terminal device, claiming that the spin-orbit torque (SOT) could rotate the Néel vector. However, in 2019, Chih-Chieh Chiang *et al*. has shown that the sawtooth signal in the AFM switching measurement might be due to the asymmetric temperature gradient in the eight-terminal device [9]. Chiang demonstrated that the sawtooth signal can be reproduced in the same device even without antiferromagnetic materials as shown in Figure 1-6. Moreover, the signal was larger in substrate with lower thermal conductivity. Therefore, the sawtooth signal might come from asymmetric temperature gradient which is not avoidable in this multi-terminal device.

doi:10.6342/NTU202301357

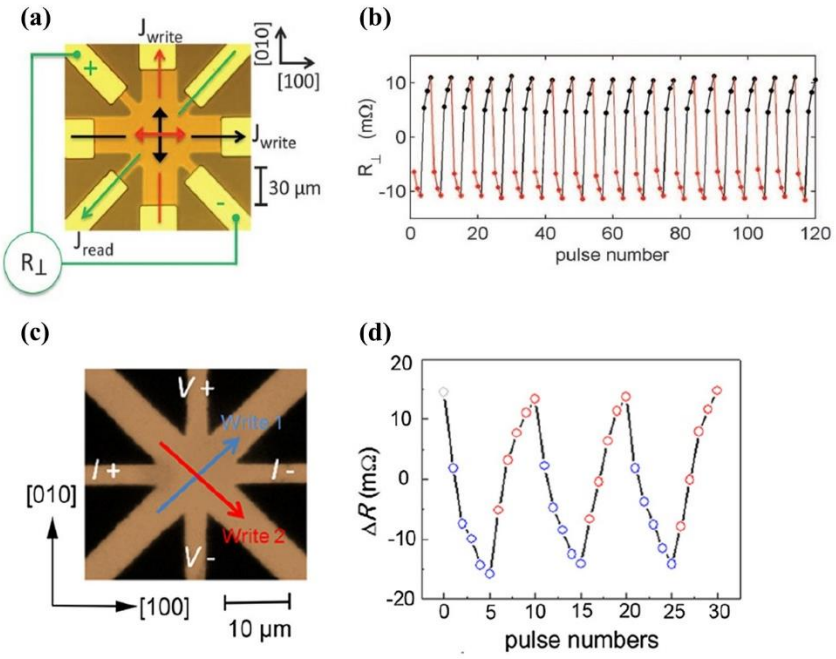

Figure 1-5: Reported AFM switching. (a) Optical image of CuMnAs eight-terminal device. The writing and reading process are sketched on the device. (c) Variation of transverse resistance after applying three consecutive writing pulse current. Revised from [7]. (c) Optical image of Pt/NiO eight-terminal device. The writing and reading process are sketched on the device. (d) Variation of transverse resistance after application of writing pulse current. Revised from [8]

doi:10.6342/NTU202301357

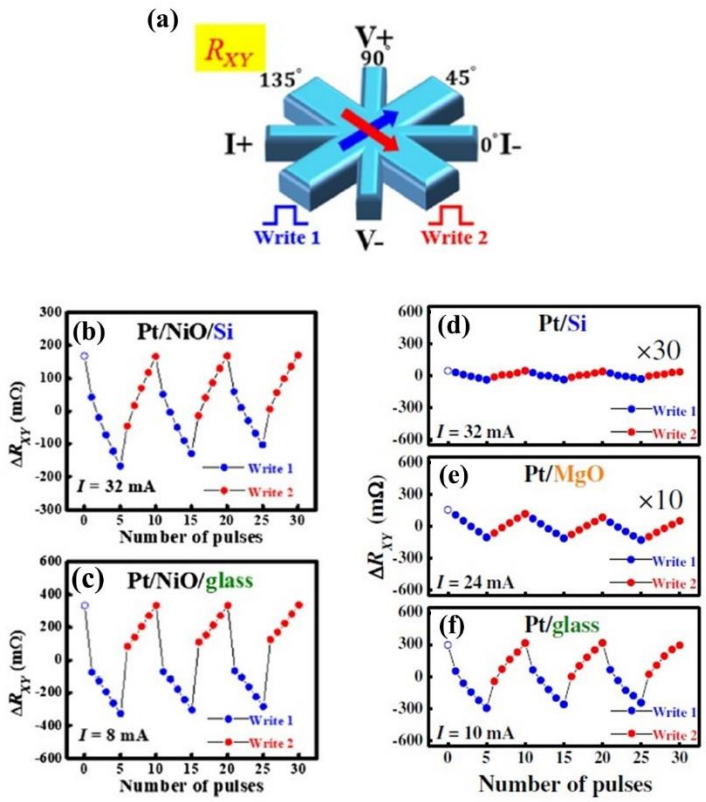

Figure 1-6: Absence of evidence of antiferromagnetic materials switching. (a) Schematic diagram of eight-terminal device and the operation processes (writing and reading). The resulting sawtooth signal in NiO growth on (b) Si and (c) glass substrate. The similar sawtooth signal was observed in non-magnetic material Pt growth on (d) S€(e) MgO, and (f) glass substrate. Revised from [9].

1.2.2 Spin-flop transition

On the other hand, an alternative approach to realize AFM switching is also needed. In 2022, Yi-Hui Zhang *et al*. has successfully manipulated the Néel vector in bulk Cr_2O_3 by the spin-flop transition and electrically detected by transverse and longitudinal resistance measurements as shown in Figure 1-7 [10]. It provides us a new platform to explore potential AFM-based spintronics. In this work, we step further toward to future applications, we grew epitaxial Cr_2O_3 thin film and tried to electrically manipulate and

doi:10.6342/NTU202301357

detect the Néel vector. The detailed experiments will be introduced in section Chapter 5 .

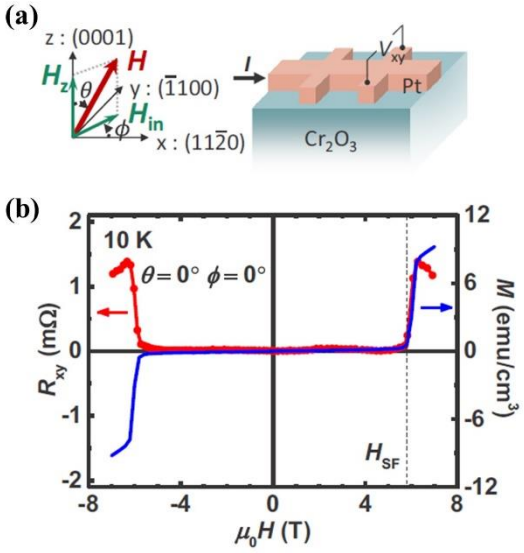

Figure 1-7: Detection of spin-flop transition by using spin Hall planar Hall effect. (a) Experimental set up (b) Field-dependent magnetization and Hall resistance R_{xy} which subtracts the background of ordinary Hall effect at 10K.

doi:10.6342/NTU202301357

1.2.3 Antiferromagnetic based neuromorphic computing device

Antiferromagnetic based spintronics might also be applied in emulating biological neural network [11,12]. An interesting work performed by Y. H. Huang *et al*. demonstrated the potential applications of ratchet-like behavior of SOT switching in the interface of antiferromagnetic material and ferromagnetic material (IrMn/CoFeB) [12]. Once the magnetization of CoFeB is switched downward (positive current), it is necessary to overcome the exchange spring effect [12]. Then, the potential energy is stored in the antiferromagnetic component [af in Figure 1-8 (d)] in IrMn. Therefore, the measured anomalous Hall resistance (R_{xy}) was variated sharply [red points in Figure 1-8 (a)] under positive current writing, resulting in digital behavior. The binary switching is useful in emulating the digital spike of neuron. On the other hand, when the magnetization is switched upward (negative current), the stored potential energy acts reciprocally. Therefore, the R_{xy} was variated gradually [blue points in Figure 1-8 (a)] under negative current writing, whose analog behavior can be used in emulating synaptic behavior. This duality of digital and analog behavior in the IrMn/CoFeB bilayer not only has benefits for neuromorphic computing but provides an opportunity of antiferromagnetic based neuromorphic computing device. This interesting work also

doi:10.6342/NTU202301357

inspires us to utilize the antiferromagnetic switching into neuromorphic computing area. Despite the sawtooth signal in eight-terminal [mentioned in section 1.2.1] has no direction evidence of AFM switching, the behavior is robust and linear due to the asymmetric temperature gradient. As mentioned previously, the repeatable and linear sawtooth signal is necessary for emulating synaptic functionalities. Even though the AFM switching might not be realized in eight-terminal device, the multi-level resistance behavior could be useful in emulating synaptic functionalities. Therefore, in this work, we build a multi-layer-multi-terminal device to emulate the synaptic functionalities including potentiation, depression, and STDP. The detailed information will be discussed in section 4.1.

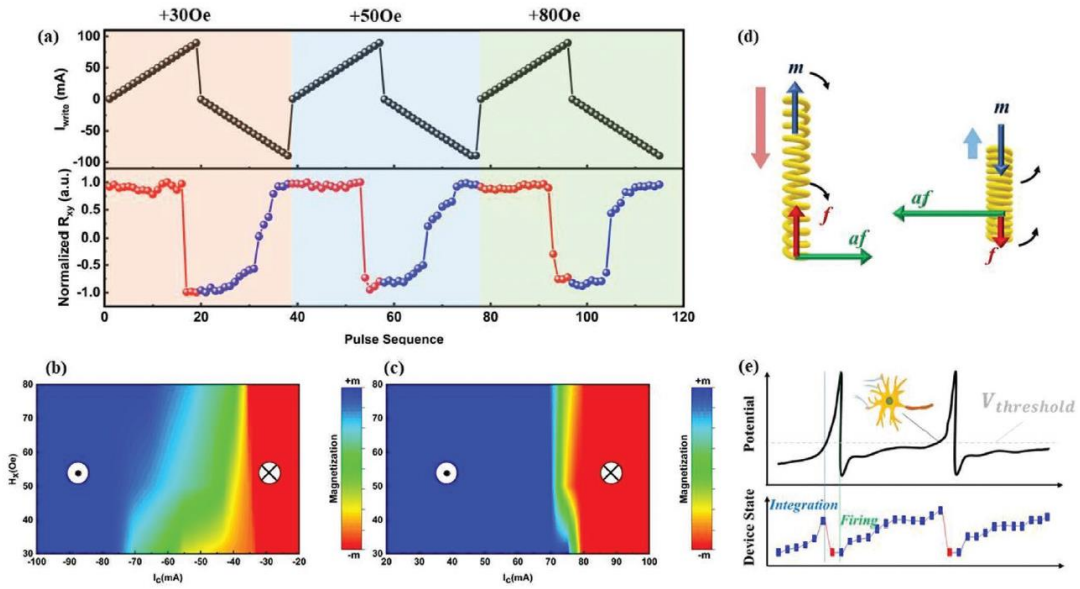

Figure 1-8: (a) Current (upper panel) induced variation of anomalous Hall effect (bottom panel). Contour of magnetic state (blue for +m, red for -m state) switched by (b) positive and (c) negative current. The two contour figures are transferred from the

doi:10.6342/NTU202301357

bottom panel in (a). (d) Ratchet-like mechanics resulted from exchange spring in IrMn/CoFeB interface. (e) Schematic diagram of neuron membrane (upper panel) and corresponding properties emulated by device (bottom panel). Revised form [12].

Chapter 2 Fundamental principle

2.1 Magnetism

Every material responds to an external magnetic field. There are five types of magnetic materials including diamagnetic, paramagnetic, ferromagnetic, ferrimagnetic, and antiferromagnetic materials. For example, diamagnetism is a property of all materials due to the Lorentz force on the electrons settling in orbits. As shown in Figure 2-1, For other types, microscopically, the key difference between these magnetism is whether and how the magnetic moments interact with each other. For example, in paramagnetic and diamagnetic materials, the magnetic moments are independent from each other. On the other hand, in ferromagnetic, antiferromagnetic, and ferrimagnetic materials the magnetic moments are coupled to each other by exchange interactions. To explicitly describe the response of magnetic materials under external magnetic field, a vector quantity of measured density of induced magnetic moment (magnetization) is defined as:

$$M(H) = -\frac{1}{V}\frac{\partial E_0}{\partial H} \tag{2.1}$$

where E_0 is the ground state energy. Or another dimensionless physical quantity

doi:10.6342/NTU202301357

(magnetic susceptibility) is introduced:

$$\chi = \mu_0 \frac{\partial M}{\partial H} = -\mu_0 \frac{1}{V} \frac{\partial^2 E_0}{\partial H^2} \quad (2.2)$$

which describe how much the materials are magnetized. The detailed explanation will be discussed in this section.

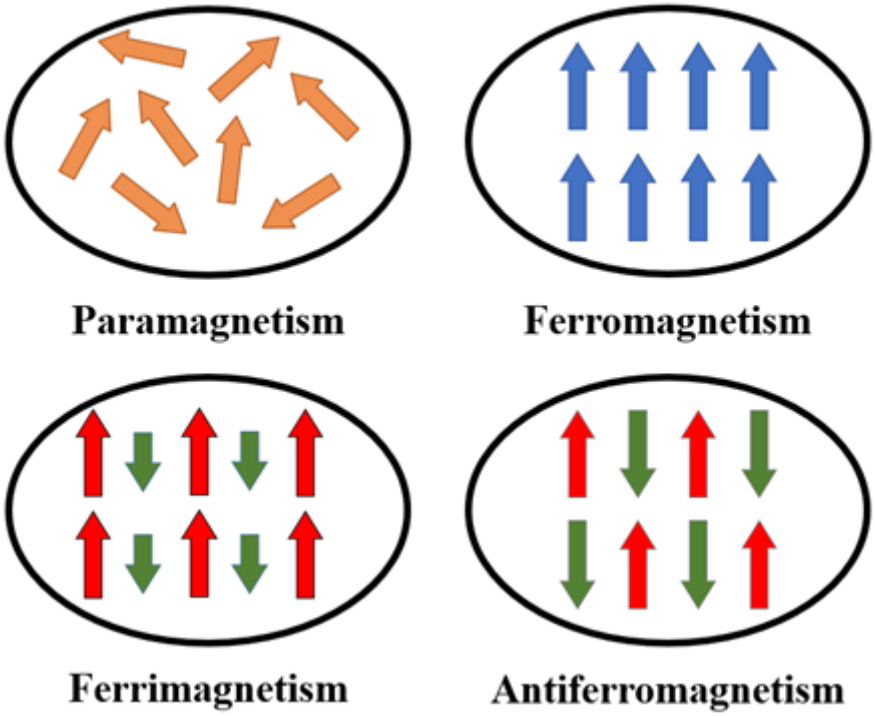

Figure 2-1: Schematic illustration for the different types of magnetism.

2.1.1 Diamagnetism

Considering an atom containing Z electrons, without exchange interaction from other atoms, the Hamiltonian of this system under external magnetic field can be written as

doi:10.6342/NTU202301357

$$\widehat{H} = \sum_{j=1}^{Z}\left[\frac{(\boldsymbol{P_j}+e\boldsymbol{A})^2}{2m_e} + V_j\right] + \frac{\mu_B g_s}{\hbar}\boldsymbol{B}\cdot\boldsymbol{S} \quad (2.3)$$

The $\boldsymbol{P_j}$ is the momentum operator and V_j is the potential energy for j[th] electron, the m_e is the mass of electron, $\boldsymbol{A}$ is the vector potential, the g_s is the g-factor, the $\hbar$ is the reduced Planck constant, μ_B is the Bohr magnetron, B is magnetic field, and S is the spin momentum operator. The second term on the right side of Eq. (2.3) is the contribution of Zeeman energy from the electron spin. By further expand the above equation, the Hamiltonian can be organized into

$$\widehat{H} = \widehat{H_0} + \frac{e^2}{8m_e}\sum_{j=1}^{Z}\left(\boldsymbol{B}\times\boldsymbol{r_j}\right)^2 + \frac{\mu_B}{\hbar}(\boldsymbol{L} + g_s\boldsymbol{S})\cdot\boldsymbol{B} \quad (2.4)$$

The L is the angular momentum operator and $\boldsymbol{r_j}$ is the position operator for j[th] electron. The second term on the right side of Eq. (2.4) corresponds to the diamagnetic response and the third term corresponds to the paramagnetic response. It is worthy to mention that for the d and f shell filled atoms, the paramagnetic term vanishes since S = L = J = 0. Therefore, only the diamagnetic term remains in such atoms: Ag, Cu, and Au. The diamagnetic term comes from the circular motion of electrons. When electron moves around nucleus, it can be viewed as a tiny current loop. This circular motion induces a magnetic field and forms a magnetic moment due to the Ampere's law. After applying a magnetic field to the materials, the magnetic flux in this tiny current loop increases. According to the Lentz's law, the current loop tends to induce a magnetic field against the change of magnetic flux. Thus, magnetic moments anti-parallel to the external

doi:10.6342/NTU202301357

magnetic field are induced in materials. As a result, the magnetization is inversely proportional to field as presented in Figure 2-2 (a). Assuming the magnetic field is applied in z-direction, the resulting magnetic susceptibility:

$$\chi = \mu_0 \frac{\partial M}{\partial H} = -\frac{n_V e^2 \mu_0}{6 m_e} \sum_{j=1}^{Z} \langle r_j^2 \rangle \tag{2.5}$$

where n_V is density of atoms μ_0 is the permeability in vacuum. It is negative and independent of temperature as shown in Figure 2-2 (b). Note that for atoms with unfilled shells, the paramagnetic term dominates, and the diamagnetism can be neglected. Generally, the susceptibility of diamagnetic materials is $\sim 10^{-15}$. Hence, although diamagnetism exists in every materials, the materials are called diamagnetic materials when they present only diamagnetism [13].

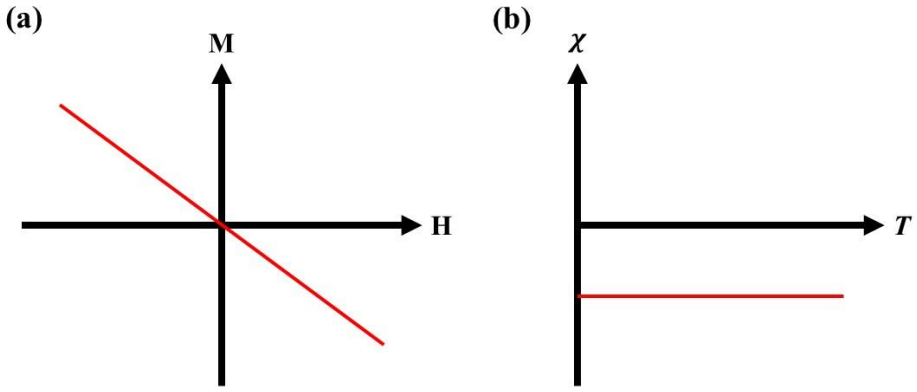

Figure 2-2: Schematic diagram of (a) M-H curve and (b) χ-T curve in diamagnetic materials

doi:10.6342/NTU202301357

2.1.2 Paramagnetism

For atoms with unfilled shells, the third term on the right side of Eq. (2.4) survives under magnetic field. In the absence of external magnetic field and at finite temperature, the magnetic moments of paramagnetic materials are randomly oriented by thermal fluctuations. After applying an external magnetic field, magnetic moments tend to align with the field. The resulting susceptibility

$$M_{para} = \frac{n_V \mu_0 \mu_{eff}^2}{3k_B T} H \rightarrow \chi_{para} = \frac{n_V \mu_0 \mu_{eff}^2}{3k_B T} \tag{2.6}$$

The μ_{eff} is effect moment and k_B is the Boltzmann constant. This formula is called Curie's law of paramagnetism and is inversely proportional to temperature.

For paramagnetic metal, we should also consider a free electron gas with equal numbers of spin-up and spin-down electrons and the resulting net magnetization is zero. As shown in Figure 2-4, the density of state of spin-up and spin-down are the same. After applying a magnetic field along the up direction, these two density of state are shifted inversely due to different Zeeman energy. From Eq. (2.4), the magnitude of the energy shift can be obtained:

$$\Delta E = \frac{\mu_B}{\hbar} g_s \boldsymbol{S} \cdot \boldsymbol{B} = \pm \mu_B \mu_0 H \tag{2.7}$$

Since the Fermi level should be the same for different spin electrons, the density of electrons can be modified:

$$n_\uparrow : \frac{n}{2} \rightarrow \frac{n}{2} + \frac{1}{2} g(E_F) \mu_B \mu_0 \tag{2.8}$$

doi:10.6342/NTU202301357

$$n_{\downarrow}: \frac{n}{2} \rightarrow \frac{n}{2} - \frac{1}{2} g(E_F)\mu_B\mu_0 \tag{2.9}$$

Therefore, the resulting susceptibility is:

$$\chi_{para} = g(E_F)\mu_B^2\mu_0 = \frac{3n_V}{2E_F}\mu_B^2\mu_0 \tag{2.10}$$

which is called Pauli paramagnetic susceptibility.

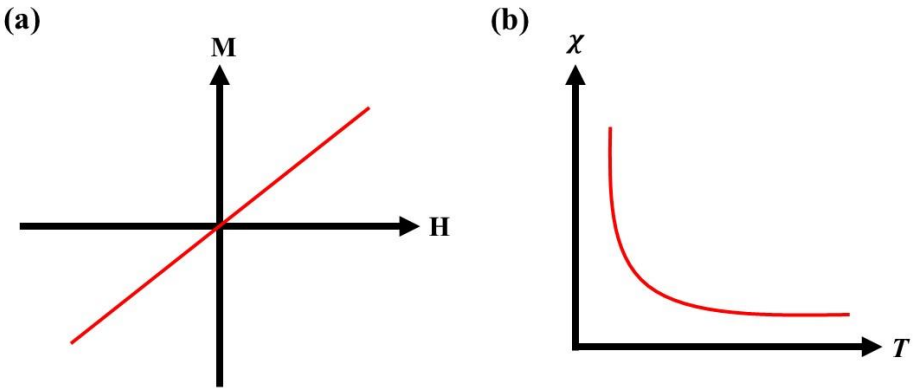

Figure 2-3: Schematic diagram of (a) M-H curve and (b) χ-T curve in paramagnetic materials

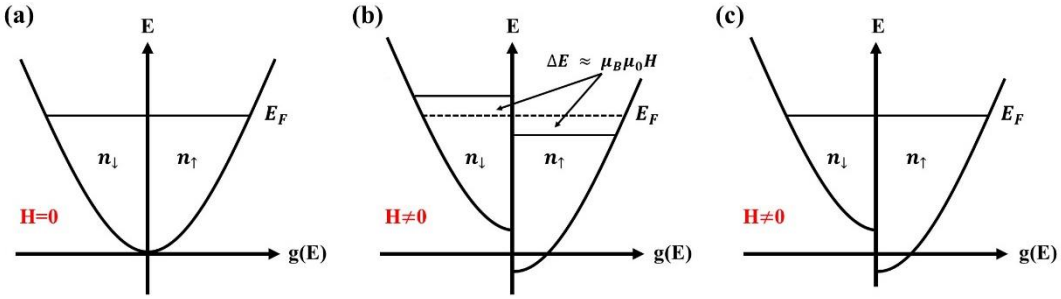

Figure 2-4: Schematic diagram of density of state in Pauli paramagnetism under magnetic field.

doi:10.6342/NTU202301357

2.1.3 Exchange Interaction

To introduce ferromagnetism, antiferromagnetism, and ferrimagnetism, we need to mention exchange interaction first. In such magnetisms, the magnetic moments are coupled to each other through exchange interaction of electron. Exchange interaction originated from the quantum mechanical nature of electron (Pauli exclusion principle). Particularly, the exchange interaction in magnetism is direct exchange interaction which is due to the overlapping of wavefunctions of electrons. According to Pauli exclusion principle, the two electrons cannot occupy the same quantum state simultaneously. The resulting wavefunction can be represented into anti-bonding (asymmetric spatial part and symmetric spin part) state or bonding state (symmetric spatial part and asymmetric part). The spin part in anti-bonding state is triplet state whose total spin angular momentum is 1. On the other hand, the spin part in bonding state is singlet state whose total spin angular momentum is 0. Thus, the effective Hamiltonian related to spin information of two electrons can be derived:

$$\widehat{H}_{eff} = -2J\boldsymbol{S_1}\cdot\boldsymbol{S_2}\ (J \equiv \frac{E_S - E_A}{2\hbar^2}) \tag{2.11}$$

where E_s is the energy of bonding state, E_A is the energy of anti-bonding state, J is defined as the exchange coupling constant, and S_1 and S_2 are the effective total angular momentum, respectively. Generally, for materials contain more than two

doi:10.6342/NTU202301357

electrons, the Hamiltonian can be expressed as:

$$\hat{H} = -\sum_{ij} J_{ij} \boldsymbol{S_i} \cdot \boldsymbol{S_j} \tag{2.12}$$

which is known as the Heisenberg Hamiltonian. The exchange coupling constant J can be either positive or negative. The sign of J determines the type of magnetism [13].

2.1.4 Ferromagnetism

For ferromagnetic materials, the electrons are coupled to each other through positive exchange interaction ($J > 0$). The system prefers the triplet state which the spins are parallel to each other. The parallel alignment results in spontaneous magnetization even without external magnetic field. If we further focus on single spin in the system, the nearest spin in the system creates an internal field acting on the spin of interest. The corresponding field is defined as mean field in Weiss molecular field theory and can be derived as:

$$H_{mf} = \frac{2J}{\mu_0 g \mu_B} \sum_j S_j = \frac{2zJ}{\mu_0 g \mu_B} \langle S_j \rangle \tag{2.13}$$

where z represents the number of nearest spin, assuming they contribute most of the coupling. If we further introduce the definition of magnetization $M = n_V g \mu_B \langle S_j \rangle$, the mean field can be written as:

$$H_{mf} = \left[\frac{2zJ}{\mu_0 n_V (g\mu_B)^2} \right] M = \lambda M \tag{2.14}$$

where λ is known as Weiss molecular field constant which is a unitless constant and

doi:10.6342/NTU202301357

is directly related to exchange interaction. If we consider the molecular field term in paramagnetic magnetization and solve for M and we can obtain the resulting susceptibility:

$$\chi_{ferro} = \frac{C}{T-T_C} \left(C = \frac{n_V \mu_0 \mu_{eff}^2}{3k_B}\right) \tag{2.15}$$

where C is known as Curie constant and $T_C = \lambda C$ is Curie temperature. From Eq. (2.15), we can observe that the ferromagnetic materials experience a phase change with respect to temperature, the resulting magnetization is shown in Figure 2-5 (b). At T_C, ferromagnetic materials experience a phase transition from paramagnetic state (high temperature) to ferromagnetic state (low temperature). In addition, in ferromagnetic state, the spontaneous magnetization forms small domains which are randomly oriented to minimize the internal energy without magnetic field as presented in Figure 2-6 (a). With the application of magnetic field, the walls between domains are moved to form bigger domains. In Figure 2-6 (b), under higher field, all domains are reoriented and align with the field, reaching to the saturated magnetization (M_s). The variation of magnetization in ferromagnetic materials under magnetic field are known as the hysteresis loop as shown in Figure 2-5 (a). However, as field gradually decreases to zero, the net magnetization is still non-zero. This non-zero magnetization at zero field after applying a large field is known as residual magnetization (M_r). To demagnetize the residual magnetization, we need to apply additional negative field to overcome it,

doi:10.6342/NTU202301357

the field is called coercive field (H_c). This phenomenon is widely used in hard disk drive as elements of memory [13].

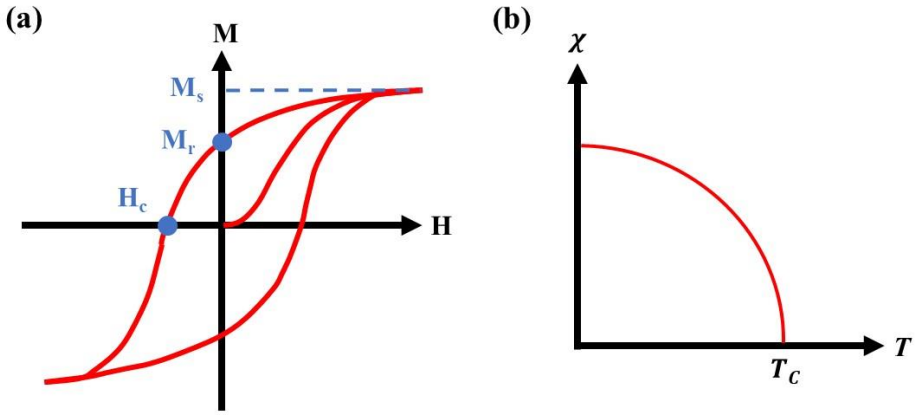

Figure 2-5: Schematic diagram of (a) M-H curve and (b) χ-T curve in ferromagnetic materials

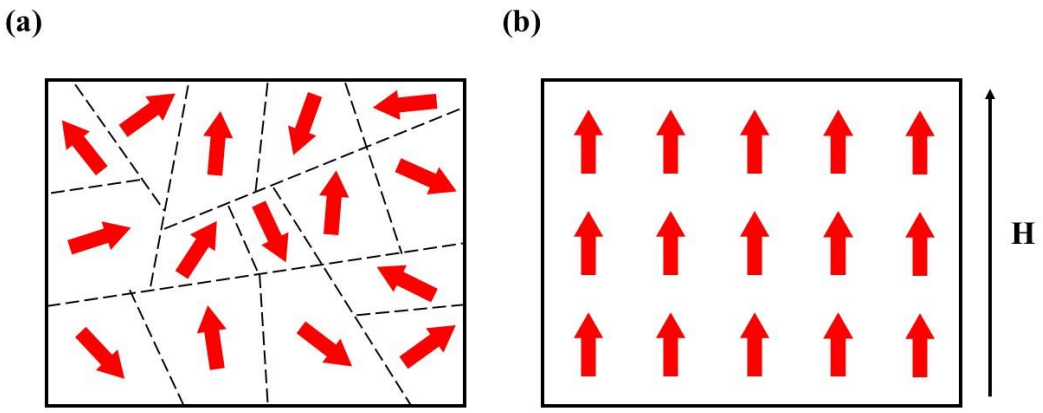

Figure 2-6: Illustration of magnetic domain in ferromagnetic materials. (a) Domain wall of ferromagnetic materials under zero magnetic field. (b) Magnetic domain configuration under external magnetic field.

doi:10.6342/NTU202301357

2.1.5 Antiferromagnetism

Antiferromagnetism is another magnetism which involves exchange interaction between the electron spins. The exchange interaction in antiferromagnetic materials is negative ($J < 0$), the system prefers the singlet state where the spins are antiparallel to each other. The magnetic moments with the same magnitude are antiparallel to each other resulting in zero magnetization and this magnetic moment orientation is known as the Néel vector. We can describe the antiferromagnetism by considering the simplest model which contains two sublattice A and B. The magnetizations with the same magnitude but antiparallel to each other $M_A = -M_B$. This antiparallel alignment of spins resulting in 0 net moment is defined as the Néel vector. Then, we adopt the Weiss molecular field theory and assuming the nearest sublattice dominates the internal interaction, the internal fields experienced by the two sublattices are shown below:

$$H_{mf}^{A} = -\lambda M_B \; ; \; H_{mf}^{B} = -\lambda M_A \tag{2.16}$$

Antiferromagnetism is like ferromagnetism, it also has a phase transition temperature between paramagnetic state and antiferromagnetic state, which is called Néel temperature (T_N). For $T > T_N$, similar to ferromagnetic case, the temperature dependent magnetization can be obtained with negative internal field:

$$M_A = \frac{C_A}{T}(H_{ext} - \lambda M_B) \tag{2.17}$$

$$M_B = \frac{C_B}{T}(H_{ext} - \lambda M_A) \tag{2.18}$$

doi:10.6342/NTU202301357

Furthermore, we assume that $C = C_A = C_B$, $T_N = C\lambda$, and we can derive the antiferromagnetic susceptibility from definition:

$$\chi_{antiferro} = \frac{2C}{T + T_N} \quad (2.19)$$

As the temperature increases above T_N, the susceptibility is reversely proportional to temperature but with negative intercept with temperature as shown in Figure 2-7 (a). However, below T_N, the susceptibility depends on the direction of external magnetic field with respect to Néel vector. In solid, the Néel vector prefers to align a certain crystallographic direction without a magnetic field. One can image this anisotropic behavior is caused by a hypothetical field, called anisotropy field (H_A). This field can act on each sublattice to pin the magnetic moments along one axis which is known as east axis such as the c-axis in uniaxial AFM Cr_2O_3. For perpendicular (H $\perp$ Néel vector) case, the magnetic field tends to align the Néel vector against the exchange interaction. In equilibrium, the resulting susceptibility is $\chi_\perp = \frac{1}{\lambda}$, which is independent of temperature as shown in Figure 2-7 (b). For parallel case (H $\parallel$ Néel vector), the magnetic field does not change the orientation of spin. In Figure 2-7 (b), the susceptibility is proportional to temperature since the thermal fluctuation disturb the Néel vector less at low temperature [13].

doi:10.6342/NTU202301357

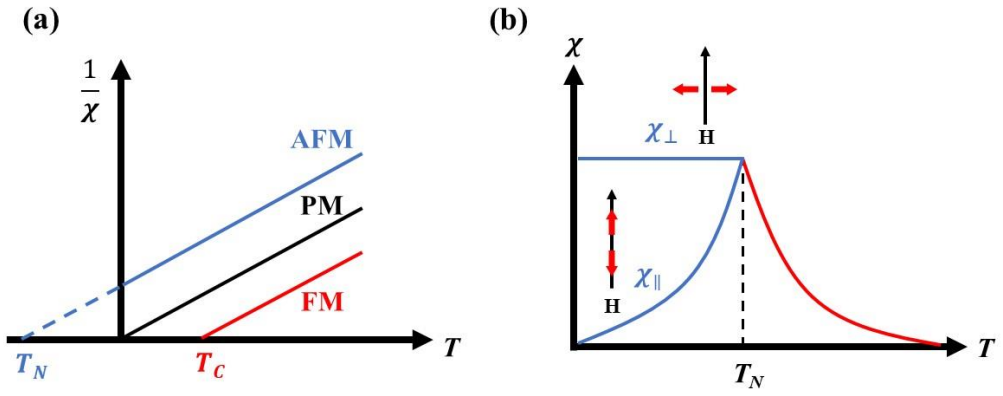

Figure 2-7: (a) Comparison of inverse susceptibility of PM, AFM, and FM. (b) Illustration of parallel susceptibility ($\chi_{\parallel}$) and perpendicular susceptibility ($\chi_{\perp}$). The definition of $\chi_{\parallel}$ and $\chi_{\perp}$ are shown as insert.

2.1.5.1 Spin flop and spin slip

When one compares anisotropic field (H_A) with exchange field (H_E), in general, there are two types of metamagnetic transitions in antiferromagnetic materials, which are spin flop and spin flip. When applying magnetic field parallel to easy axis, two cases may happen regarding to large or weak anisotropy filed comparing exchange interaction. For $H_E > H_A$, once the field compensates the anisotropy field, the Néel vector will be rotated to perpendicular state with respect to easy axis. Energetically, magnetic field perpendicular to easy axis is more stable than the parallel case. After this transition, the Néel vector is canted increasingly by magnetic field and the net magnetization is proportional to field. This transition is known as spin-flop transition as shown in Figure

doi:10.6342/NTU202301357

2-8 (a). The spin-flop transition happens under critical field which the energies of perpendicular and parallel configurations are equal.

$$-2M_\alpha H_A - \frac{1}{2}\chi_\parallel H_{SF}^2 = -\frac{1}{2}\chi_\perp H_{SF}^2 \quad (2.20)$$

In the above equation, the M_α is sublattice magnetization. Therefore, the spin flop field can be obtained:

$$H_{SF} = \sqrt{\frac{4M_\alpha H_A}{\chi_\perp - \chi_\parallel}} \quad (2.21)$$

As field keeps increasing, the magnetization would be completely aligned with the field to the saturation state. In the case of bulk Cr_2O_3, the spin flop field is 5.8 T, and the saturation field is estimated to be 500 T. For $H_E < H_A$, , the Néel vector will be flip and aligned with the field directly and the net magnetization jumps from zero to saturation as shown in Figure 2-8 (b) [14,15].

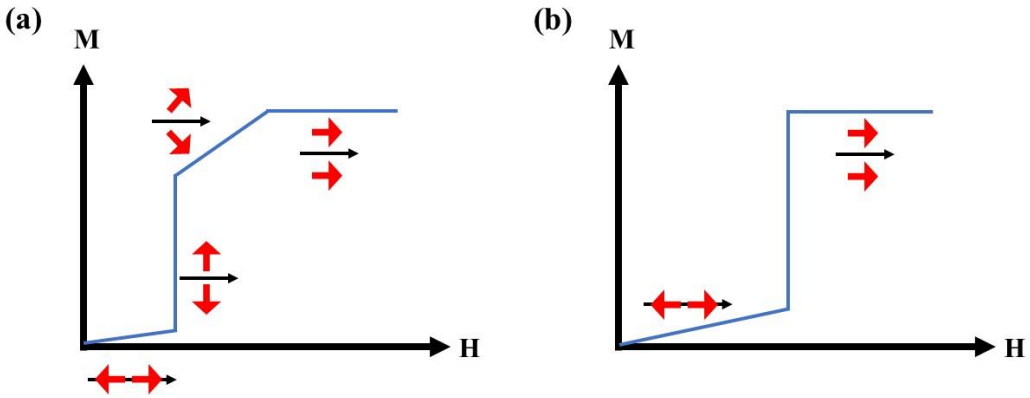

Figure 2-8: Schematic diagram of processes of (a) spin flop and (b) spin flip under magnetic field

doi:10.6342/NTU202301357

2.1.6 Ferrimagnetism

Ferrimagnetism is similar to antiferromagnetism. Due to negative exchange interaction, the magnetic moments prefer to align antiparallelly. However, the magnitude of magnetization of the two sublattice are different ($|M_A| \neq |M_B|$) resulting in non-zero total magnetization as shown in Figure 2-9. Therefore, the behavior of M-H curve is like ferromagnetism.

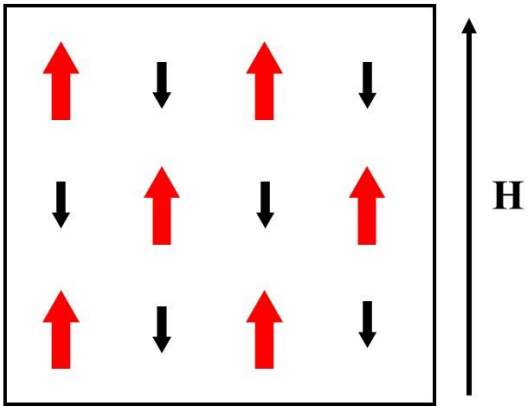

Figure 2-9: Schematic diagram of ferromagnetism.

2.2 Spin current

A flow of electrons produces an electrical charge current which is related to the electric property of electrons (e = -1.6 $\times$ 10^{-19} coulomb). In addition, there is another intrinsic property found in the development of quantum mechanics, which is the spin.

doi:10.6342/NTU202301357

Spin is an intrinsic angular momentum of electron, which is different from the orbital angular momentum due to orbital motion. Unlike charge current, the spin current which is spin-polarized current carries the spin angular momentum. The most efficient spin current is pure spin current where the electron with opposite spin moving in opposite direction as presented in Figure 2-10. A charge current usually contains a lot of electrons and their spin orientations are random, the resulting total angular momentum is zero. To generate pure spin current, the spin Hall effect (SHE) is one of the most important mechanisms. In this section, I will introduce these effects explicitly.

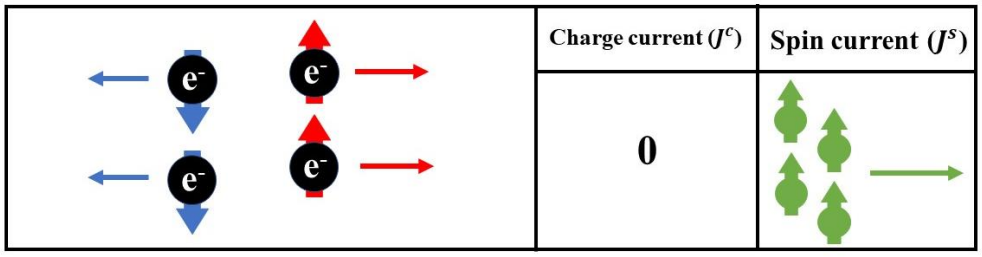

Figure 2-10: Schematic diagram of pure spin current

2.2.1 Spin Hall effect (SHE) and inverse spin Hall effect (ISHE)

The ordinary Hall effect describes the electron accumulation in transverse direction due to the Lorentz force. In SHE, even without magnetic, when electrical

doi:10.6342/NTU202301357

current pass through normal metals, electrons with opposite spin accumulates in the opposite/transverse direction due to the spin-orbit coupling (SOC) [16-19]. Since the same amount of spin-up and spin-down electrons are separated in transverse direction, the charge current is cancelled.

The SHE which proposed by D'yakonov and Perel' in 1971 is a relativistic effect between orbital motion and spin of electrons [19,20]. As shown in Figure 2-11 (a), in the reference frame of a proton, the electron moves circularly around the proton. This orbital motion of an electron generates a magnetic field on the proton. In the reference frame of an electron, the electron is fixed, and the proton moves circularly as presented in Figure 2-11 (b). Thus, the circular motion of a proton produces an effective magnetic field and affects the motion of electron and interact with the spin. The SOC in the case of single electron and proton is relatively small compared to other effects in solid state physics. The physicists suggest the SOC could be large in heavy metal (HM). Due to SOC in normal metal, the electrons with opposite spin in injecting charge current will be deflected in opposite direction resulting in pure spin current. The schematic procedure is shown in Figure 2-12 (a). Since the number of electrons get deflected are the same, it is impossible to detect the pure spin current directly by electrical measurement. On the other hand, the SHE is reversible where the spin current can also generate charge current by SOC. This counterpart of SHE is called inverse spin Hall

doi:10.6342/NTU202301357

effect (ISHE). As shown in Figure 2-12 (b), the injection of spin current can produce charge current in normal metal. Thus, ISHE is a very powerful tool to detect pure spin current.

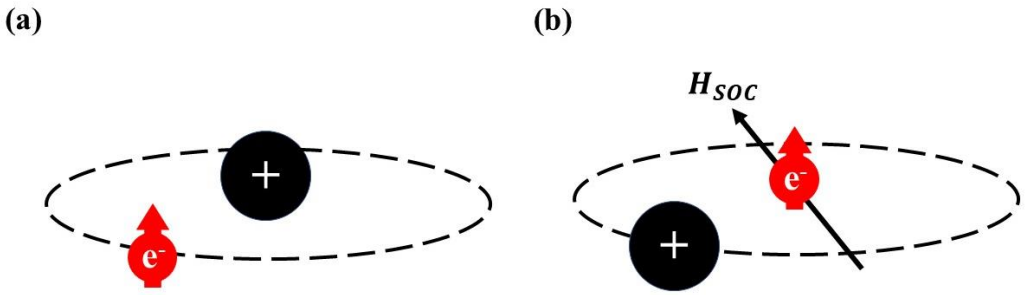

Figure 2-11: Schematic diagram of spin-orbit coupling (SOC). (a) Reference frame of proton, an electron orbiting proton. (b) Reference frame of electron, a proton orbiting electron. The black arrow represents the SOC field acting on electron.

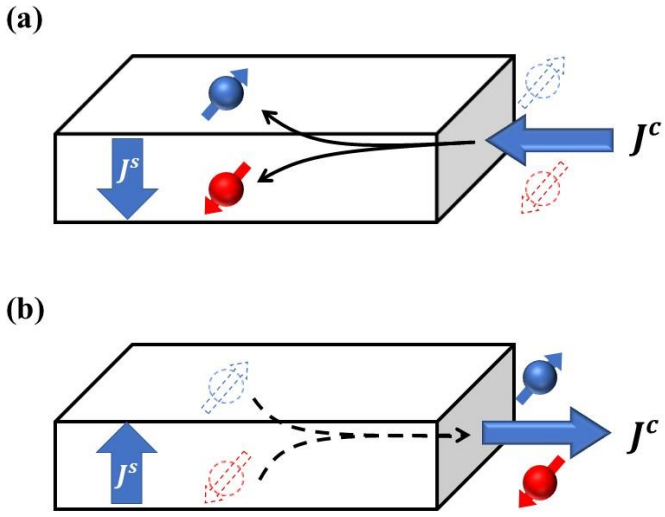

Figure 2-12: Schematic illustration of (a) spin Hall effect (SHE) and (b) inverse spin Hall effect (ISHE).

doi:10.6342/NTU202301357

2.3 Neural network

2.3.1 Biological neural network

Our brain is an extremely complex system which can parallelly process a lot of data and information with low energy consumption (~20W). The biological neural network contains two fundamental parts which are the neurons and synapses as shown in Figure 2-13. Neurons are composed of a cell body, an axon, and dendrites. A synapse is a cleft between a post-synaptic dendrite, a pre-synaptic axon. Neurons are responsible for information processing like the CPU in conventional computer. The information processing between neurons is completed through the generation and conduction of action potential (spike) [3]. The neurons transmit information which is encoded into spike through axon into the body cell of next neurons through dendrites. In this complex network, a neuron can receive spike from many neurons and transmit spike to many neurons building up a comprehensive network. The spikes from other neurons result in changing in voltage potential across the neuron's cell membrane. When the voltage reaches certain threshold voltage, the cell body generates an action potential which transmits along the neuron's axon [3].

doi:10.6342/NTU202301357

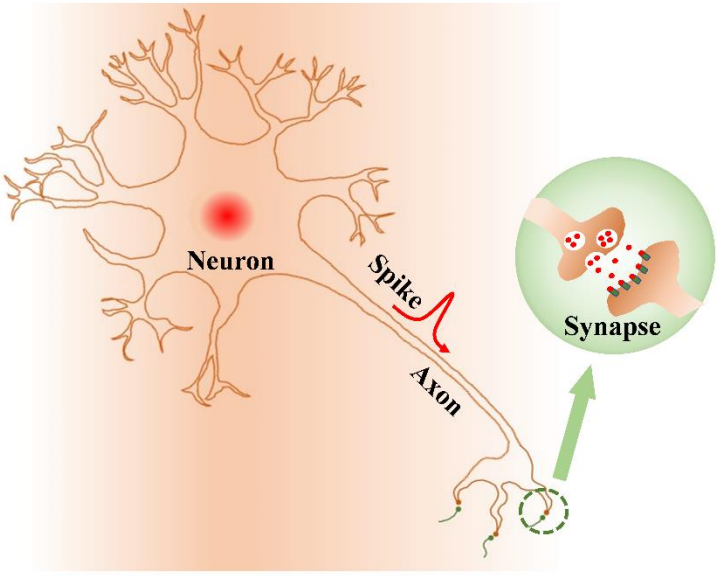

Figure 2-13 Schematic illustration of the biological neural network.

Synapses are the storage elements and employed to transmit and integrate the processed spikes between neurons. Synapse which is believed to be the most important part defines the connection strength (synaptic weight) between neurons. The synaptic weight is reconfigured based on the relative timing (denoted as $\Delta t_{post\text{-}pre}$) and/or the sequence of spikes between pre- and post- synaptic neurons. These behaviors of variance in synaptic weight are called spike-timing dependent plasticity (STDP) which is critical in information processing. Additionally, depending on different functionality of human brain, different kinds of STDP are employed. As shown in Figure 2-14. In anti-symmetric STDP, if the post-synaptic neuron fires a spike immediately after the pre-synaptic neuron fires a spike ($\Delta t_{post\text{-}pre} > 0$), the synaptic weight is enhanced since this event follows the causality. On the contrary, if the pre-synaptic neuron fires a spike

doi:10.6342/NTU202301357

immediately after the post-synaptic neuron fires a spike ($\Delta t_{post\text{-}pre} < 0$), the synaptic weight is decreased since this event violates the causality. Moreover, if $|\Delta t_{post-pre}|$ is relatively large, the synaptic weight would remain unchanged since the connection between the neurons is weak. In symmetric STDP, the synaptic modification only depends on the relative timing but not on the order. With STDP, neurons embedded in neural networks are able to integrate input signals and transform them into a meaningful output even though the meanings themselves are not strictly known by the neurons [21].

doi:10.6342/NTU202301357

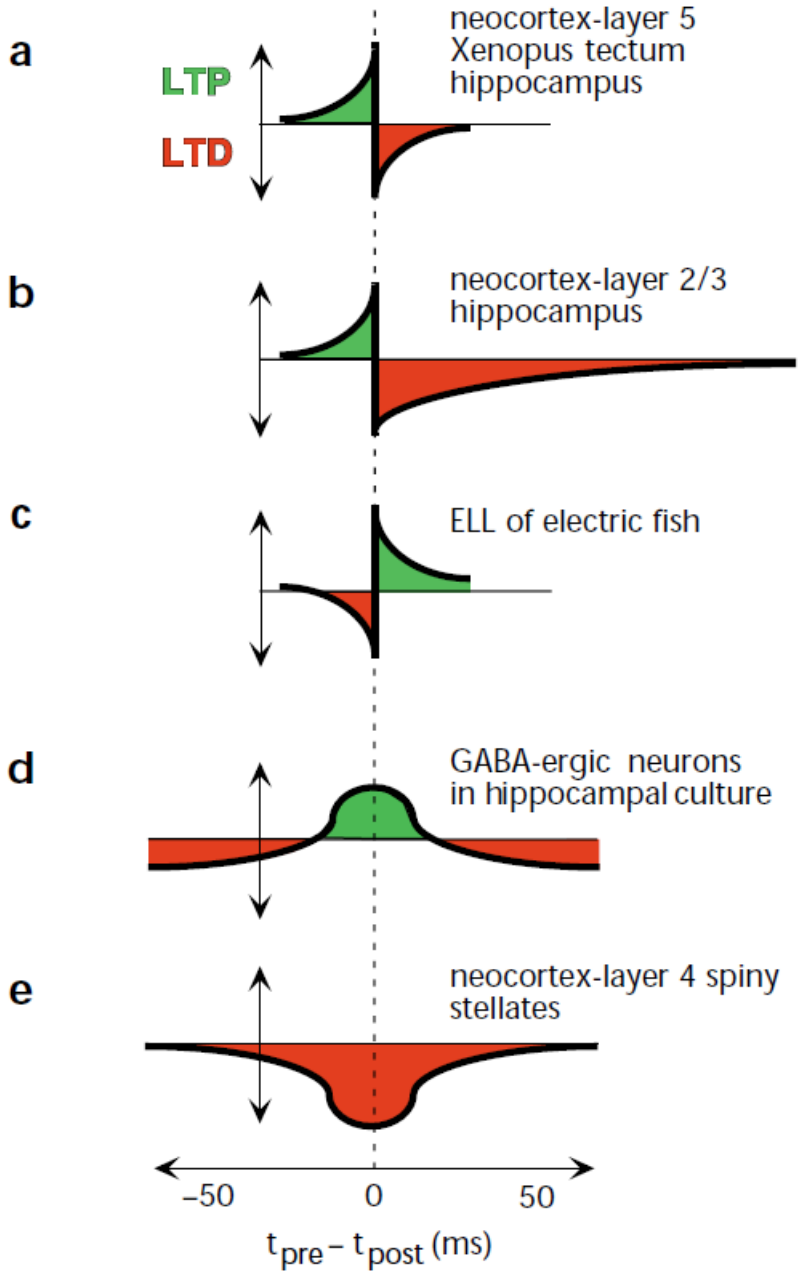

Figure 2-14 Various types of synaptic modification (STDP) evoked by repeated pairing of pre- and post-synaptic spikes in different preparations. Revised from [22].

doi:10.6342/NTU202301357

2.4 AFM switching

2.4.1 Eight-terminal devices

During the past years, people are working on reducing the power consumption and shrinking the scale of device. One efficient way is developing spintronics which drives and controls devices through pure spin current. The ferromagnetic spintronics have been developed such as magnetoresistive random-access memory (MRAM) which creates two magnetoresistance state through different spin orientation of the two adjacent ferromagnetic layer [23-25]. However, as the scale shrinking down to nanoscale, the parasitic stray magnetic field effect (mutual influence of neighbor magnetic domain) is impossible to ignore [26]. The stray magnetic field causes non-uniformity and significantly influences the magnetic properties of MRAM. Therefore, physicists have proposed to utilize antiferromagnetic materials which have zero magnetization, ultrafast dynamics, zero stray field, and is robust against magnetic perturbations. More interestingly, it has been suggested that one may be able to manipulate (switching) and detect the Néel vector through pure spin current.

The first experimental exploration of AFM switching was published in 2016, conducting in antiferromagnetic CuMnAs [7]. It was predicted that Néel-order spin-orbit torque could be generated by electrical current in inversion symmetry breaking

doi:10.6342/NTU202301357

AFM materials even without a heavy metal spin current source layer due to inverse spin galvanic effect. Then, based on spin-orbit torque, a crossbar device was then proposed to realize the AFM switching via SOT through two perpendicular writing current and the resulting switching of Néel vector can be detected by anisotropic magnetoresistance (AMR) [27]. Although CuMnAs crystal has inversion symmetry, Mn atoms form two sublattices [see Figure 2-15 (a)] which are inversion symmetry breaking counterparts. Therefore, the inverse spin galvanic effect still generates locally nonequilibrium spin polarizations of opposite sign in the two sublattices. As shown in Figure 2-15 (a), the eight-terminal device was used in AFM switching in CuMnAs. As mentioned in Figure 2-15 (b), the writing process is done by applying three consecutive pulse current with 50 ms width and $J_{write} = 4 \times 10^6\, Acm^2$ amplitude through [010] (red arrow and red data points) and [100] (black arrow and black data points) crystal axis. The reading process is done by measuring the transverse resistance after each writing pulse current. In Figure 2-15 (c), after every writing pulse current the resulting transverse resistance changed discretely and different direction of writing process results in opposite change of transverse resistance, resulting in sawtooth-like behavior. Additionally, each writing process created the same incremental change, which might imply each writing process rotate or switch a small AFM domain. However, there is no direct evidence for the switching of AFM domain by SOT in this eight-terminal device. Unlike conventional

doi:10.6342/NTU202301357

spin-orbit torque (SOT) and spin-transfer torque (STT) switching in FM system, when injecting current is larger than a critical current ($J > J_c$) the resistance change is quickly saturated and irreversible. The current induced magnetization switching can be further confirmed by field measurement. Even more surprisingly, it has been demonstrated that the sawtooth signal can be reproducible even without any antiferromagnetic materials in the eight-terminal device [9,28-32]. The detailed information will be discussed in section 2.4.2. Hence, the real electrical AFM switching is still open to discussion.

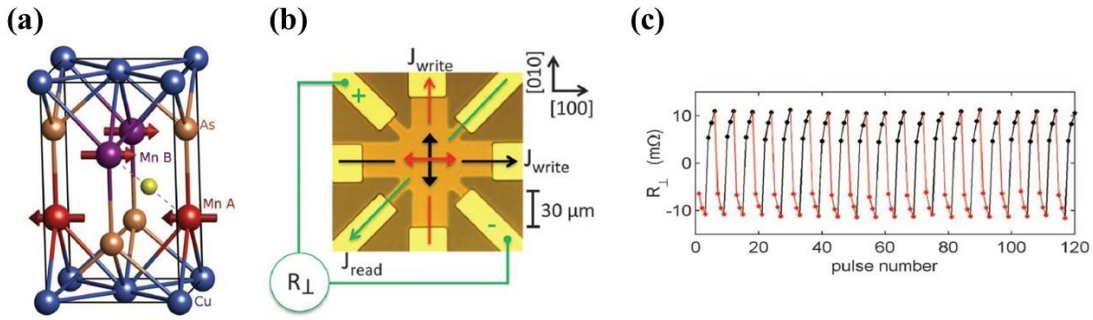

Figure 2-15: (a) Crystal structure of CuMnAs and AFM ordering. Two Mn (purple and red) atoms form two sublattices which are inversion counterparts. (b) Optical image of the eight-terminal device. The currents in writing and reading process are sketched on the device. (c) Variation of transverse resistance after applying three consecutive writing pulse current with 50 ms width and $J_{write} = 4 \times 10^6\ Acm^2$ amplitude. The black data points presented the writing process of black current line in panel D and the red data points presented the writing process of red current line. The green current line is for the reading process of anisotropic magnetoresistance (AMR). Revised from [7].

doi:10.6342/NTU202301357

2.4.2 Non-magnetic origin

In 2019, our group, Chih-Chieh Chiang found out that the sawtooth signal in the eight-terminal comes from the asymmetric temperature gradient due to the multi-terminal structure [9]. In Chiang's work, the similar sawtooth signal was reproduced in antiferromagnetic NiO which fabricated into the same eight-terminal device as shown in Figure 2-16. However, the sawtooth signal remains when the AFM layer is removed [see Figure 2-17]. Moreover, the magnitude of the sawtooth signal increases when the devices are fabricated on substrate with lower thermal conductivity ($\kappa_{Si} > \kappa_{MgO} > \kappa_{glass}$).

doi:10.6342/NTU202301357

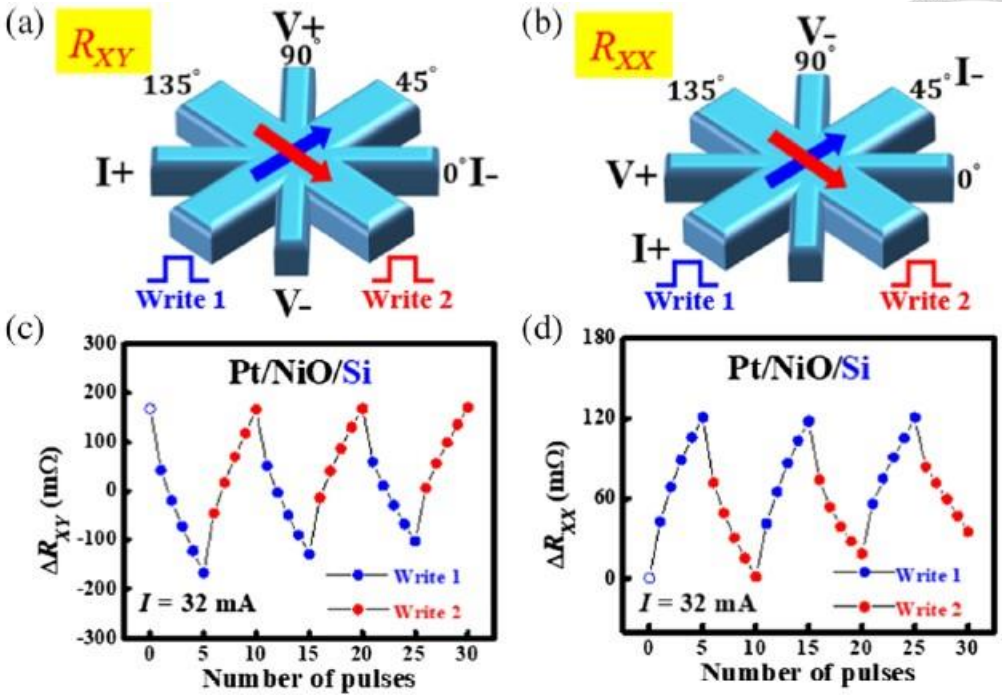

Figure 2-16: Schematic diagrams of eight-terminal devices used in published paper [9] for (a) transverse resistance and (b) longitudinal resistance measurements. The writing and reading processes are sketched in the diagram. Writing pulse currents with 10 ms width and 32 mA amplitude are applied through write 1 or write 2 terminal. The relative changes of (c) transverse resistance (ΔR_{XY}) and (d) longitudinal resistance (ΔR_{XX}) are measured by 2 mA reading current. Revised from [9].

It indicates that this current-driven switching measurement in the eight-terminal devices might be contaminated by unavoidable thermal artifacts. The COMSOL simulations of temperature distribution after applying one-shot of pulse current through different terminal were performed. After applying a pulse current, the device will be heated up asymmetrically and create a temperature gradient inside the device as shown in Figure 2-18. Due to this temperature gradient, the electron injected by the reading current will be deflected and result in a resistance change in the transverse direction. As number of pulse current increases, the change of transverse resistance also increases.

doi:10.6342/NTU202301357

In addition, when the pulse current was injected from different terminal, the resulting temperature gradient was different. Consequently, the similar sawtooth signal can be observed even without antiferromagnetic materials. What is more, after this work, more work related to the non-magnetic origin of the AFM switching in the eight-terminal devices were conducted [28-32]. More unavoidable artifacts due to the high current density writing process were found in the same eight-terminal devices. Thus, an alternative way for electrical AFM switching is needed. In my work, we tried to use spin-flop phenomenon in Cr_2O_3 to realize the AFM switching, which will be discussed in Chapter 5 .

On the other hand, the sawtooth signal might be contaminated by asymmetric temperature gradient, but the signal is very robust, linear, and easy to control. This might be useful in neuromorphic computing which requires a tunable physical quantity to emulate the functionalities of synapse. The detailed information will be discussed in Chapter 4 .

doi:10.6342/NTU202301357

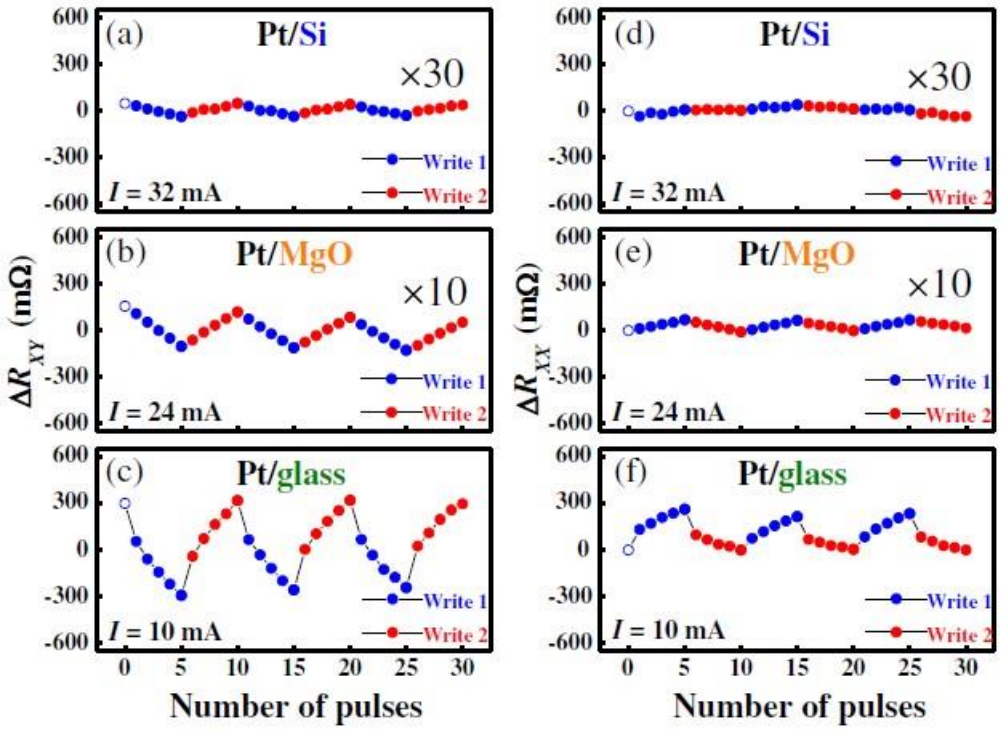

Figure 2-17: The values of ΔR_{XY} and ΔR_{XX} of nonmagnetic Platinum which growth on (a, d) Si, (b, e) MgO, and (c, f) glass substrate are collected from the same eight-terminal device and writing process with different amplitudes of writing pulse current. Revised from [9].

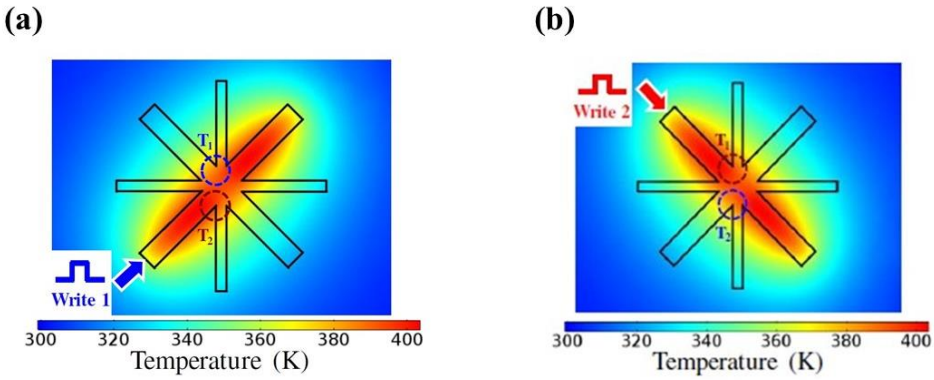

Figure 2-18: COMSOL simulation of temperature distribution in the Pt/glass eight-terminal devices after applying one-shot writing pulse current of density $1.75 \times 10^7\ A/cm^2$ through (a) write 1 and (b) write 2 terminal. Revised from [9].

doi:10.6342/NTU202301357

2.4.3 Detection and manipulation of Néel vector in bulk Cr_2O_3

Cr_2O_3 is a uniaxial antiferromagnetic insulator (T_N ~ 310K) with hexagonal structure whose Néel vector prefers to align along c-axis. In Cr_2O_3, the crystal anisotropic effective field (H_A) is 700 Oe and antiferromagnetic exchange coupling effective field (H_E) is 245 T [33]. For the larger exchange coupling, the spin-flop transition in Cr_2O_3 is predicted and can be estimated to be 5.8 T. In 2022, our group, Yi-Hui Zhang *et al*. have successfully demonstrated how to detect and manipulate the Néel vector by spin-flop transition in bulk Cr_2O_3 [10].

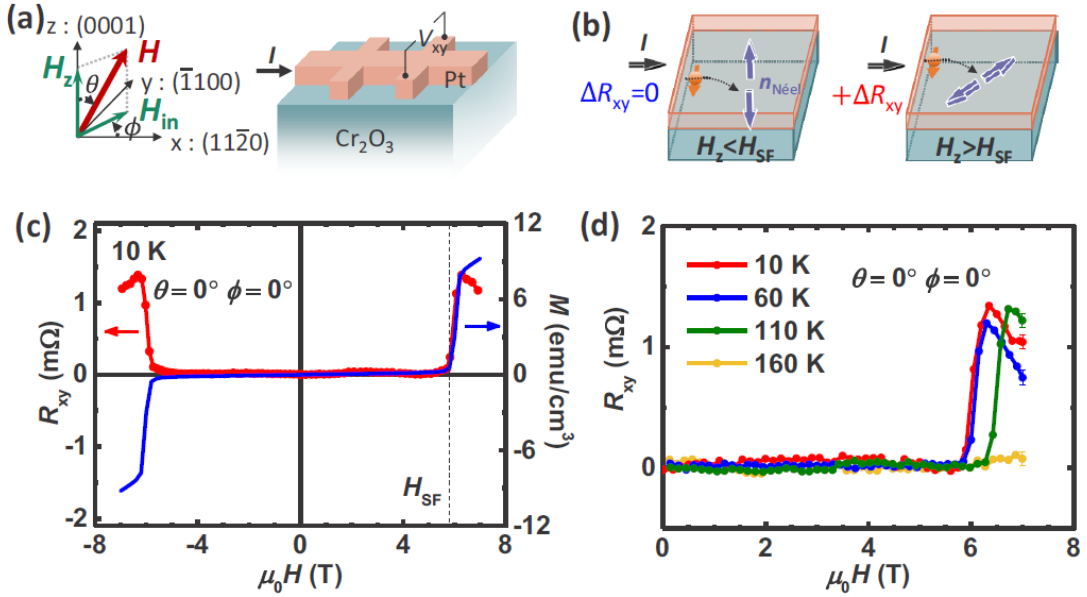

Figure 2-19: (a) Experimental setup of spin Hall planar Hall measurement on (0001)-oriented Cr_2O_3 single crystal with 5 nm Pt Hall bar. (b) Illustration of the transport properties before and after spin-flop transition. (c) Hall measurement at 10 K

doi:10.6342/NTU202301357

(subtracting ordinary Hall background). (d) Hall measurement under different temperatures. Revised from [10].

As shown in Figure 2-19 (c), the magnetization jumps suddenly which is relating to the flop of Néel vector. The Néel vector coherent rotation also can be detected by both Hall and resistance measurement. As presented in Figure 2-19 (c), the Hall resistance of the Pt jumps symmetrically under magnetic field. This symmetric transition can be described by spin Hall planer Hall effect. The pure spin current is injected perpendicularly from the top Pt layer, and if the angle between magnetic moment and spin index σ is not 0° or 90°, there is nonzero planer Hall resistance. In Cr_2O_3, once the magnetic field along z-axis is larger than 5.8 T, the Néel vector is rotated 90° to x-y plane. As field increasing, the Néel vector is tilted slight along z-axis and generate net magnetic moment which contributes to nonzero planer Hall resistance. Moreover, this transition also can be detected by longitudinal resistance measurement as shown in Figure 2-20. This phenomenon can be explained by spin Hall magnetoresistance. Once the spin index σ of spin current from Pt layer is perpendicular to the Néel vector, the spin current will be absorbed. On the other hand, if σ is parallel to the Néel vector will be reflected. The reflected spin current will generate charge current through inverse spin Hall effect, resulting in resistance in longitudinal direction. Moreover, they also demonstrate the manipulation of Néel vector after the spin-flop transition as presented

doi:10.6342/NTU202301357

in Figure 2-21. During the measurement, the magnetic field was intentionally tilted an angle θ which create an in-plane field. After the spin-flop transition, the Néel vector lays in x-y plane and is perpendicular to H_{in} due to lowest Zeeman energy. Therefore, the Néel vector can be rotated by a very small in-plane field. As presented in Figure 2-21 (a), the resulting R_{XY} is opposite with the opposite sign of angle $\emptyset$ (blue and red curve). For $\emptyset$ = 0, the Néel vector is now along $(\bar{1}100)$ which is also parallel to the spin index of injected spin current, resulting in zero R_{xy}.

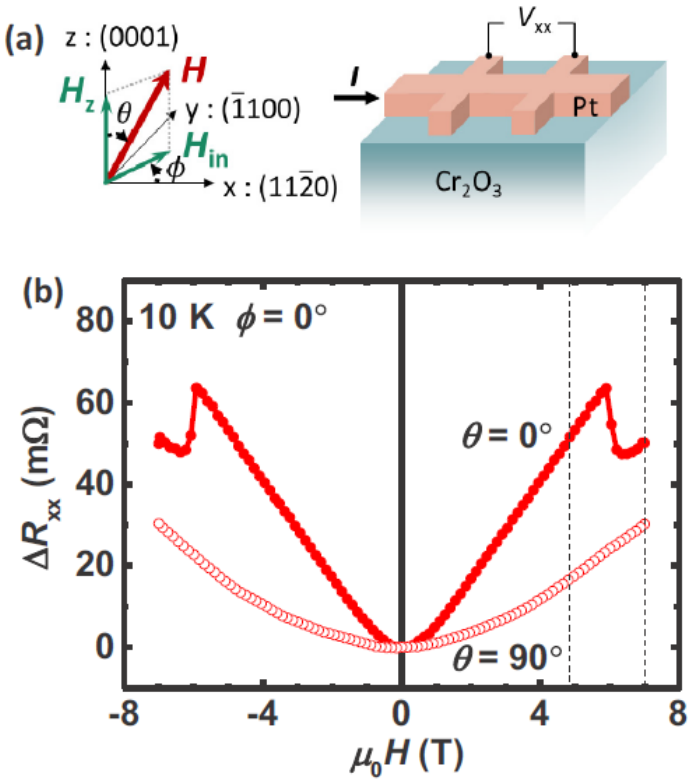

Figure 2-20: Detection of spin-flop transition by spin Hall magnetoresistance measurement. (a) Experimental for the spin Hall magnetoresistance measurement. (b) Field dependent magnetoresistance R_{xx}. Revised from[10].

doi:10.6342/NTU202301357

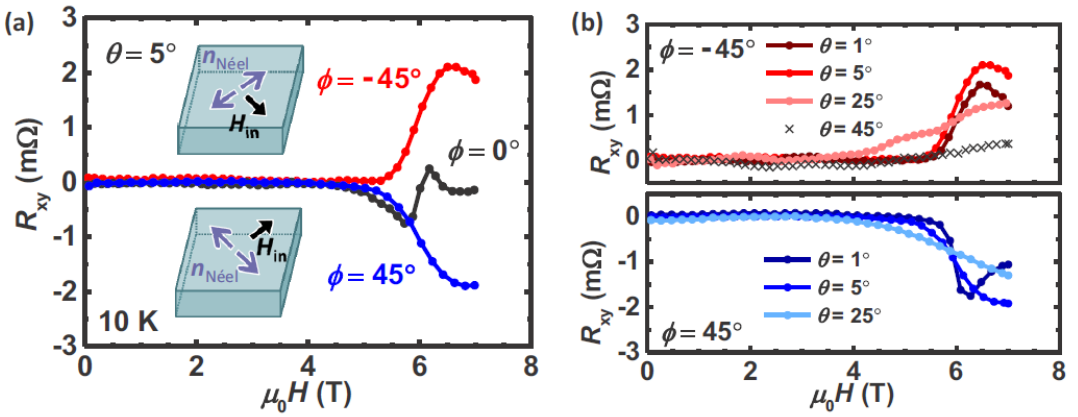

Figure 2-21: Manipulation of Néel vector by magnetic field with different θ and $\emptyset$ angles. (a) Experimental data with the angle $\theta = 5°$. The resulting in plane field (H_{in}) is 6100 Oe with 45° (red curve), 0° (black curve), and -45° (blue curve). (b) Experimental data with different tilting angle θ. Revised from [10].

It is fascinating that the Néel vector can be electrically detected and manipulated in Cr_2O_3. It provides us a platform to explore antiferromagnetic spintronics. But the previous result was demonstrated in bulk Cr_2O_3, which is impossible to achieve zero field electrical switching. In this work, we tried to grow epitaxial thin film and electrically field-free detected and manipulate the Néel vector. Moreover, we try to use pure spin current to control the spin-flop transition. The detailed information will be discussed in section Chapter 5 .

doi:10.6342/NTU202301357

Chapter 3 Experimental Methods

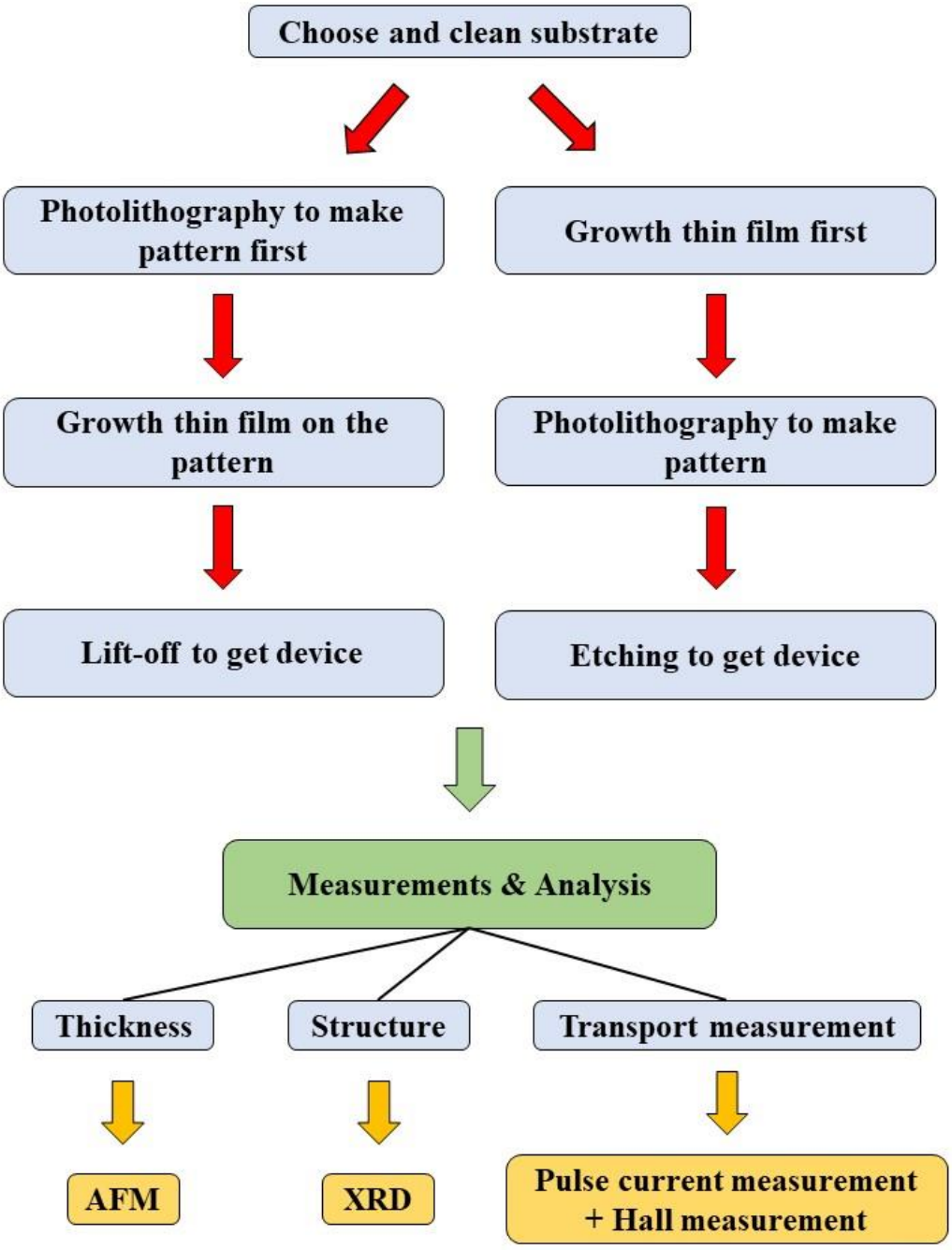

Figure 3-1: Overview of experimental procedures

doi:10.6342/NTU202301357

3.1 Thin film and device fabrication

3.1.1 Photolithography

In this work, we grow thin films on the different substrates and fabricate into multi-terminal pattern devices. As sketched in Figure 3-1, there are two different ways to fabricate the devices: lift-off or etching process. Based on the different shape of devices, different fabrication processes are adopted. In both processes, photolithography is important. Photolithography is widely used in semiconductor industry, allowing electronic devices to process in small dimension and high density. In photolithography, the key tool is a light-sensitive materials called photoresist which is usually divided into two categories: positive and negative photoresist. The difference between positive and negative photoresist is their reaction with the UV light. When positive photoresist is exposed under UV light, it becomes dissolvable in the developer solution. On the other hand, when negative photoresist is exposed under UV light, it becomes non-dissolvable in the developer solution. This difference provides us two different way to define the pattern of the devices.

The first one is the lift-off process; the schematic procedures are shown in Figure 3-2. We first drip a few drops of positive photoresist on the substrate and rotate it with certain speed (1500 rpm for 10 s, then 4500 rpm for 30 s) to make a uniform and flat

doi:10.6342/NTU202301357

photoresist film. Secondly, we heat the substrate with photoresist under $110°C$ for 50 s to improve the adhesion of photoresist. Then, we put this sample into exposure machine with cover of the mask which has certain pattern allowing UV light to expose certain region of photoresist. After exposure, the dissolvable and non-dissolvable mixture of photoresist is formed. Next, we put this sample into developer and the dissolvable part is dissolved leaving the certain pattern of photoresist on the substrate. If we further grow thin film on this sample, the materials would be deposited vertically on the pattern. Finally, we can use acetone to develop the whole photoresist, leaving the thin film with certain pattern on the substrate.

The second one is etching process, where the negative photoresist is adopted. Since the reaction of negative photoresist with UV is opposite with positive photoresist, the procedure is also opposite. In etching process, the thin film is first deposited on the substrate and the negative photoresist is dripped on it. The etching process removes materials uniformly on the substrate and the negative photoresist is then a protection of film from etching. After etching, we can use acetone to develop the remaining photoresist, leaving the thin film with certain pattern on the substrate.

Generally, both lift-off and etching process can fabricate the same device. But for some special materials, they require annealing process during thin film growth, the annealing process would destroy the photoresist. Therefore, positive photoresist is not suitable for

doi:10.6342/NTU202301357

these materials.

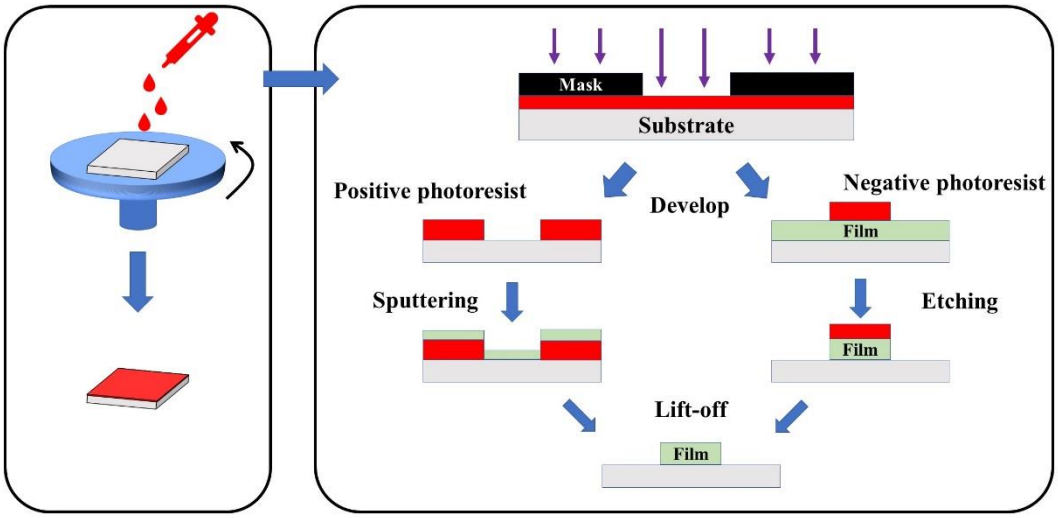

Figure 3-2: Schematic diagram of procedures in photolithography

3.1.2 Magnetron sputtering system

In this work, we use magnetron sputtering to grow thin films and combine with the photolithography mentioned previously to fabricate devices. In this section, I will introduce the basic physics of sputtering and then introduce our sputtering system. Sputtering is one kinds of physical vapor deposition (PVD) and widely used to grow various materials (metal, semiconductor, and insulator) with high speed and high uniformity. The general procedures is summarized in Figure 3-3, the ionized atoms bombard the target and eject the atoms which then deposit on the substrate.

In the high-vacuum chamber (10^{-8} ~ 10^{-9} Torr in our chamber), we first input small amount of Argon (Ar) gas (1~10 mTorr), since it is inert gas which do not react

doi:10.6342/NTU202301357

chemically with sputter target. Additionally, we apply high DC electric field between the target (materials want to deposit) and substrate. The electric field will accelerate a trait of free electrons, causing the collision between electrons and Ar atoms. This collision induces dissociation and ionization of Ar atoms, and then the plasma is generated inside the chamber [Figure 3-3 (a) to (b)]. This plasma is a high-energy gas-like phase consisting of Ar^+ ions, Ar atoms, and electrons. Meanwhile, the liberated electrons from Ar atoms will also be accelerated and participate another ionization process as shown in Figure 3-3 (c). Therefore, more plasma will be generated inside the chamber. Because Ar^+ ions are positive particles and target is connected to cathode, the ions will be accelerated toward the target. Then, the high-energy Ar^+ ions will bombard the target and transmit the kinetic energy to the target atoms which will then be ejected. As sketched in Figure 3-3 (d), the ejected atoms will then accumulate on the substrate and form a thin film.

However, the ejected target atoms move randomly inside the chamber, causing instability and uncertainty during sputtering. Thus, the magnetron sputtering [Figure 3-4 (a)] is then introduced to improve the stability and the deposition rate. In magnetron sputtering, multiple magnets are placed behind the target and create magnetic field. Due to this magnetic field, the plasma is confined creating higher density plasma which improves the sputtering rate. Moreover, in our magnetron sputtering system, we also

doi:10.6342/NTU202301357

grow oxide thin film by reactive sputtering. As shown in Figure 3-4 (b), during the normal sputtering process, the O_2 gas is input and takes part in the chemical reaction, simultaneously. As a result, an oxidized thin film is then deposit on the substrate. In this work, we use reactive sputtering to grow Cr_2O_3 thin films.

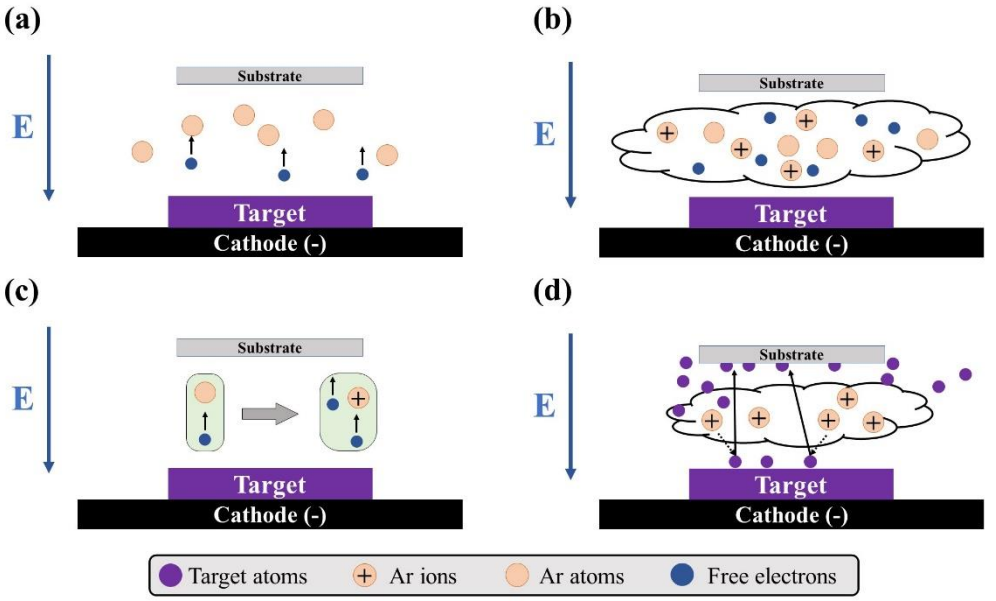

Figure 3-3: Schematic diagrams of basic sputtering processes. (a) Inside the sputtering chamber, after applying DC electric field, the free electrons gain kinetic energy. The accelerated electrons collide with Ar atoms resulting ionization and excitation. (b) After process (a), the plasma which contains electrons, Ar atoms, and Ar ions is generated. (c) The liberated electrons from Ar atoms by ionization will continue to collide with Ar atoms resulting in bigger plasma. (d) Since Ar ions are positive particles, they will be accelerated toward the target and bombard the surface of target. This process transmits kinetic energy to the target atoms and eject these atoms. The ejected atoms will then deposit on the substrate.

doi:10.6342/NTU202301357

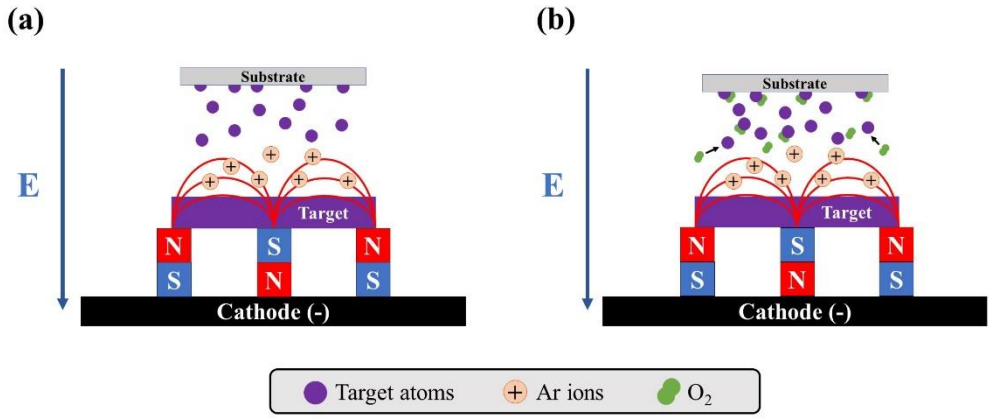

Figure 3-4: Schematic diagram of magnetron sputtering. (a) With magnets placed behind the target, the magnetic field is generated and confine the plasma, focusing the deposition process on the substrate. (b) The reactive magnetron sputtering process of oxygen gas.

3.2 Thin film characterization

3.2.1 Atomic force microscopy (AFM)

The AFM was invented by G. Binnig *et al.* in 1986 for solving the disadvantage of scanning tunneling microscopy (STM) which only can measure the surface of conducting materials [34]. In the AFM measurement as sketched in Figure 3-5 (a), a sharp tip is placed on one end of cantilever to scan the surface of sample. In addition, a laser beam is transmitted to and reflected from the cantilever to detect the deformation of cantilever. During the scanning, the van der Waal force between the tip and the surface induces a displacement and bend the cantilever, resulting a position shift to the

doi:10.6342/NTU202301357

laser beam. This shift is detected by a position-sensitive four-sectional photodiode which can detect both longitudinal and torsion bending. After that, the signal is then transport to computer for analysis. Finally, the topographical image of the surface of sample can be obtained.

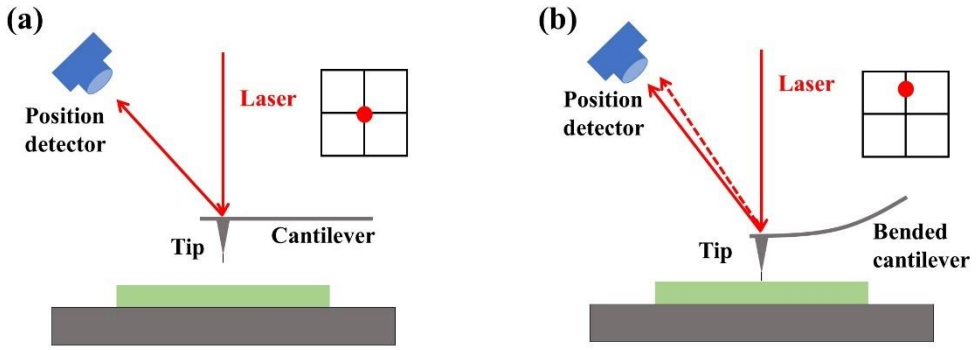

Figure 3-5: Schematic diagram of atomic force microscopy measurement. (a) Before measurement with the sample, the cantilever is not bended, thus the reflected laser is detected without position-shift (b) Once the tip closes to the sample, the cantilever is bended by the van der Waal force. Therefore, the reflected laser is detected with position-shift.

3.2.2 X-ray diffraction (XRD)

X-ray diffraction (XRD) is a very useful technique for characteristic of the crystal structure. The X-ray was first discovered by Wilhelm Röntgen in 1895. The incidence of X-ray into crystal can induce a lot of interactions such as X-ray absorption, photoemission, scattering, and diffraction. We can use these interactions to investigate

doi:10.6342/NTU202301357

different information of the crystal. In XRD, the main application is to investigate the crystal structure since the wavelength of X-ray (1.54056 Å in this work) is close to the spacing between crystal planes. The principle of XRD was developed by Lawrence Bragg and Willian Henry Bragg in 1913, which is known as the Bragg's law:

$$2dsin\theta = n\lambda \quad (3.1)$$

where n is a positive integer, d is the spacing between crystal plane, and λ is the wavelength of X-ray. From Eq. $2dsin\theta = n\lambda$ (3.1), we can know that only at certain incident angle, the diffraction can happen. Therefore, we can scan the angle θ and obtain a unique diffraction pattern which can be analyzed for detailed crystal information. Furthermore, XRD also can be used for characterized for the quality of single crystal, which is known as the rocking curve measurement as shown in Figure 3-7. The rocking curve measurement scans small angle of $\Delta\omega$ and measures the diffraction signal with the fixed detector. If the atoms of single crystal or epitaxial thin film arrange perfectly parallelly (high quality), the diffraction only occurs within extremely small angle region ($\Delta\omega$), resulting in very sharp diffraction peak. On the other hand, if the atoms arrange badly (low quality), the diffraction occurs within lager angle region, resulting in broaden diffraction peak. Therefore, after measurement, we can calculate the full width at half maximum (FWHM) to quantify the quality of the materials. The smaller value FWHM is, the higher quality the material has.

doi:10.6342/NTU202301357

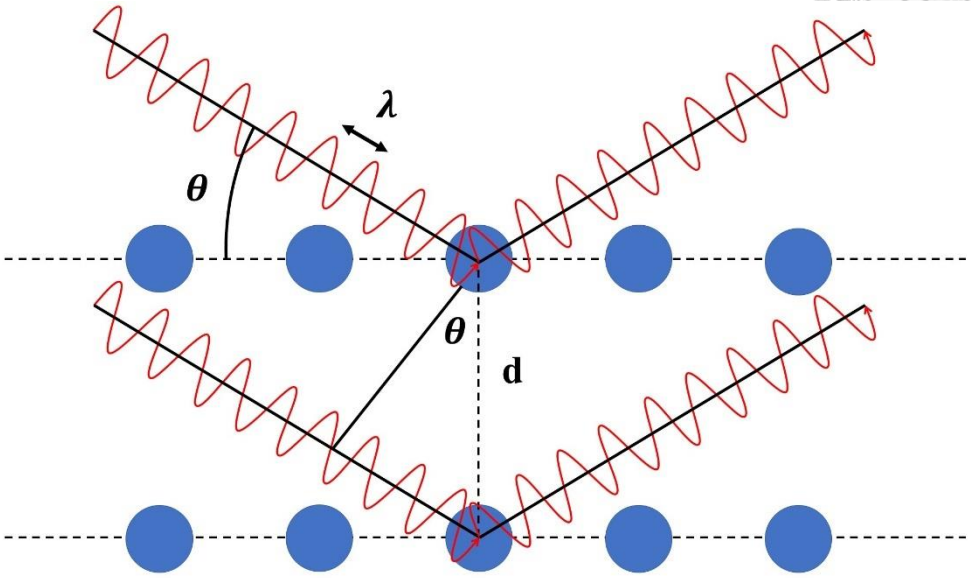

Figure 3-6: Schematic diagram of Bragg's law.

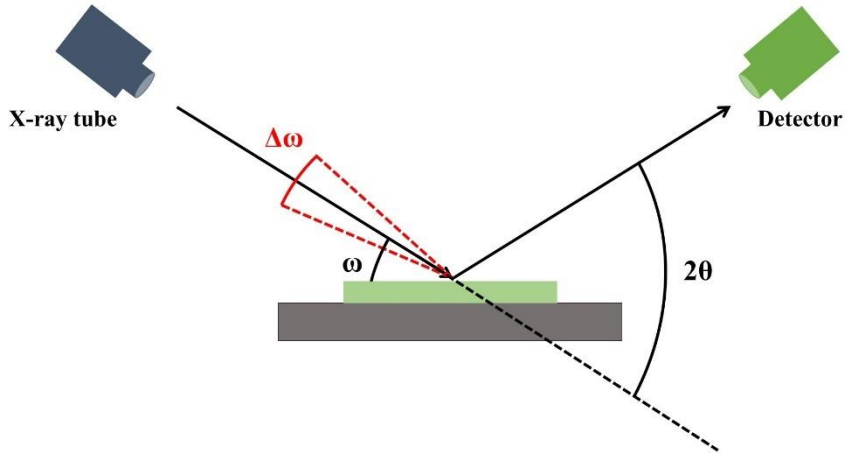

Figure 3-7: Schematic diagram of rocking curve measurement.

doi:10.6342/NTU202301357

3.3 Electrical transport measurement

3.3.1 Physical property measurement system (PPMS)

Physical property measurement system (PPMS) designed by Quantum Design provides various transport measurements with variable temperature and temperature range. In this work, our PPMS provides electrical and thermal transport measurements with magnetic field up to 7T and temperature range 1.9-400K. The liquid helium is filled in the PPMS chamber to cool down the superconducting magnetic coil and to control the environment temperature of the sample chamber. Therefore, PPMS can create a custom environment and perform transport measurements.

3.3.2 Pulse current measurement

In the operation of synaptic functionalities in the multi-layer-multi-terminal device, we employ Keithley 6221 current source, Keithley 2182A nanovoltmeter, and Keithley 2400 current source. The whole measurement is controlled by LABVIEW program and ARDUINO program. As sketched in Figure 3-8, the writing pulse current is provided by Keithley 6221 current source and is injected through the write1 or write 2 terminal.

doi:10.6342/NTU202301357

After the application of pulse writing current, the asymmetric temperature is created in the bottom layer (writing layer). Additionally, the temperature gradient transfers to the top layer (reading layer) through the middle layer (separating layer). Finally, the reading process is done by Keithley 2182A nanovoltmeter, and Keithley 2400 current source. The measured transverse resistance (R_{xy}) is defined as the synaptic weight in this neuromorphic computing device.

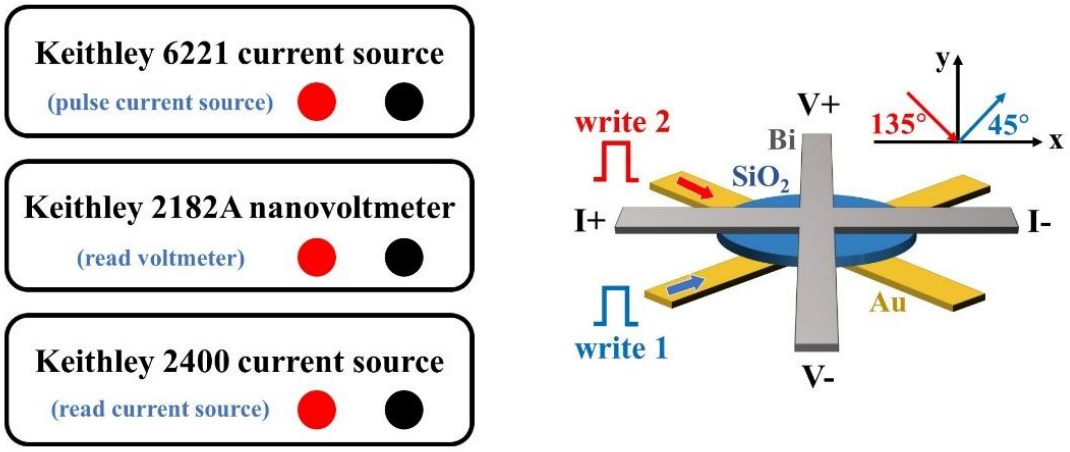

Figure 3-8: Pulse current measurement. We use Keithley 6221 current source to apply writing pulse current through write 1 and write 2 terminal. After the application of pulse current, the transverse resistance of the reading layer is measured by Keithley 2400 current source and Keithley 2182A nanovoltmeter.

doi:10.6342/NTU202301357

Chapter 4 Results and Discussion

4.1 Neuromorphic computing in multi-layer-multi-terminal device

The work in chapter 4 has been published in applied physics letter on 26 June 2023 [35].

4.1.1 Multi-layer-multi-terminal device

In this work, we present a multi-layer-multi-terminal neuromorphic computing device. As mentioned previously, the stable and linear sawtooth signal in the eight-terminal device used in AFM switching might be useful in emulating synaptic functionalities. Moreover, our previous works show that the recurring signals is not electrical switching of the AFM Néel vector but thermal effect. Thus, even without an antiferromagnet, we may be able to demonstrate a linear but more robust multi-level signals. However, some works have proposed that the high current density might cause permanent damage in the device itself [28,31]. Therefore, we separated the writing layer and reading layer to prevent the permanent change in reading layer. As shown in Figure 4-1, We first deposited Cr (5 nm)/Au (5 nm) on glass substrate to be the writing layer and fabricate it into cross-bar shape following the lift-off procedure mentioned in section 3.1.1. The 5 nm Cr is the buffer layer for better welding of thin Au on the substrate. Au has extremely low resistance and can reduce the power consumption

doi:10.6342/NTU202301357

during the writing process, which is necessary for future applications.

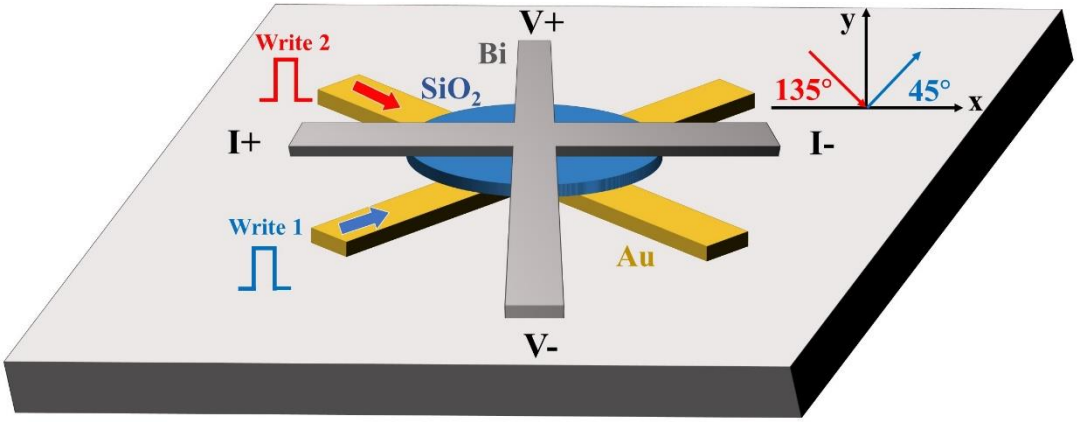

Figure 4-1: Schematic diagram of multi-layer-multi-terminal device and operations.

In addition, since the sawtooth signal is created by asymmetric temperature gradient, we use the low thermal conductivity glass to be the substrate to decrease the heat dissipation. For the reading layer, we use high Seebeck coefficient Bismuth (~72 μV/K) [36] sandwiched between Cr and Al_2O_3 [Cr (10 nm)/Bi (100 nm)/Al_2O_3 (10 nm)], where Cr is buffer layer and Al_2O_3 is the capping layer preventing oxidation. The higher Seebeck coefficient materials can generate more resistance change in transverse direction by the same amount of temperature gradient. Finally, we use an insulting SiO_2 (50 nm) to separate the writing and reading layer. This separation can also reduce the fluctuation of synaptic weight during the reading process [28,31,37,38]. In synaptic operations, we define the 45° terminal in writing layer to be the write 1 path (blue

doi:10.6342/NTU202301357

arrow) and the 135° terminal in writing layer to be the write 2 path (red arrow). The synaptic functionalities are realized by the pulse current measurement. After injecting a writing pulse current through write 1 or write 2 path, the asymmetric temperature gradient was generated in the writing layer.

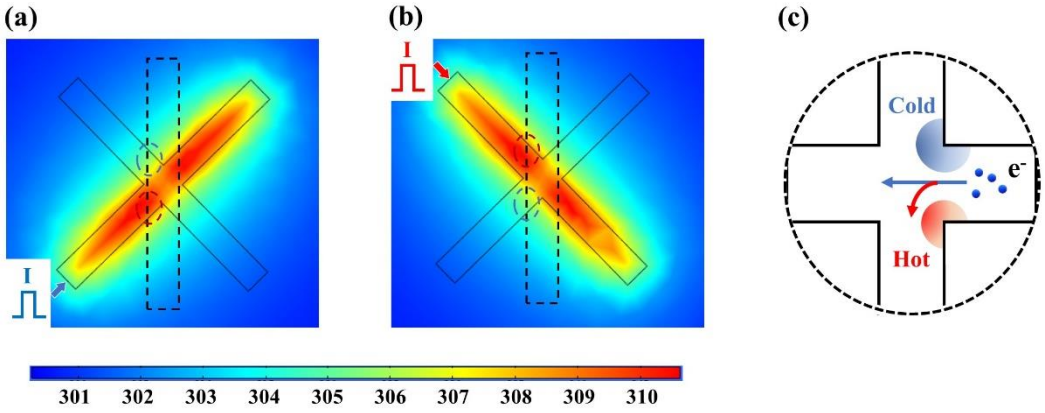

Figure 4-2: COMSOL simulation of temperature distribution of writing layer after writing pulse current 5.5×10^6 A/cm^2 is injected along (a) write 1 (b) write 2. The color bar shows the actual value of temperature distribution. (c) Schematic diagram of electrons deflected by asymmetric temperature gradient.

To explicitly characterized the asymmetric temperature gradient, we employ the COMSOL Multiphysics software to simulate the temperature distribution after injecting the writing pulse current. We perform the simulation of a injected writing pulse current with current density 5.5×10^6 A/cm^2 and duration time 100 ms through different writing paths: Figure 4-2 (a) write 1 (45°), (b) write 2 (135°), and (c) write 3 (225°). The

doi:10.6342/NTU202301357

resistivity of 2.44 $\mu\Omega$cm for Au and the thermal conductivity of 3.17 and 1.38 W/(cmK) for Au and glass substrate, respectively are used in the simulation. The results show that the heat would accumulate asymmetric temperature gradient in the device. This asymmetric temperature gradient will then transfer to the reading layer through insulting layer, which create hot zone (red circle) and cold zone (blue circle). In the reading process, we measure the transverse resistance of Bi (synaptic weight) with low reading current (1 mA). As electrons were injected into reading layer, they will be deflected by the asymmetric temperature gradient, resulting in change of transverse resistance. The symmetry of the thermal distribution from injected writing pulse current through the write 1 and write 2 paths are opposite. Therefore, the direction of the variated transverse resistance is also opposite, causing opposite variation of synaptic weight. In this work, we can inject different number of writing pulse current through different terminal to arbitrarily control the synaptic weight.

4.1.2 Potentiation and depression

In biological neural networks, the importance of synapses is the ability to variate the connection (synaptic weight) between two neurons. The synaptic weight can be persistently variated by changing the amount of neurotransmitter pre-synaptically or the amount of AMPA receptor present post-synaptically [3]. Therefore, it is necessary

doi:10.6342/NTU202301357

for artificial synapses to electronically variate its synaptic weight arbitrarily by external stimulation. In our work, we first show the linear and symmetric synaptic weight change in this device. In Figure 4-3 (a), we injected a writing pulse current (10 mA, 11 mA, and 12 mA) with 200 ms pulse width through write 2 path and measure the transverse resistance of Bi with small reading current, immediately. We calculate the ΔR_{xy} (%) = $(R_{xy}^{f} - R_{xy}^{i})/R_{xy}^{i}$, where R_{xy}^{i} and R_{xy}^{f} are the transverse resistance of Bi before and after the writing process of a single pulse, to show the difference of synaptic weight variated in writing process.

doi:10.6342/NTU202301357

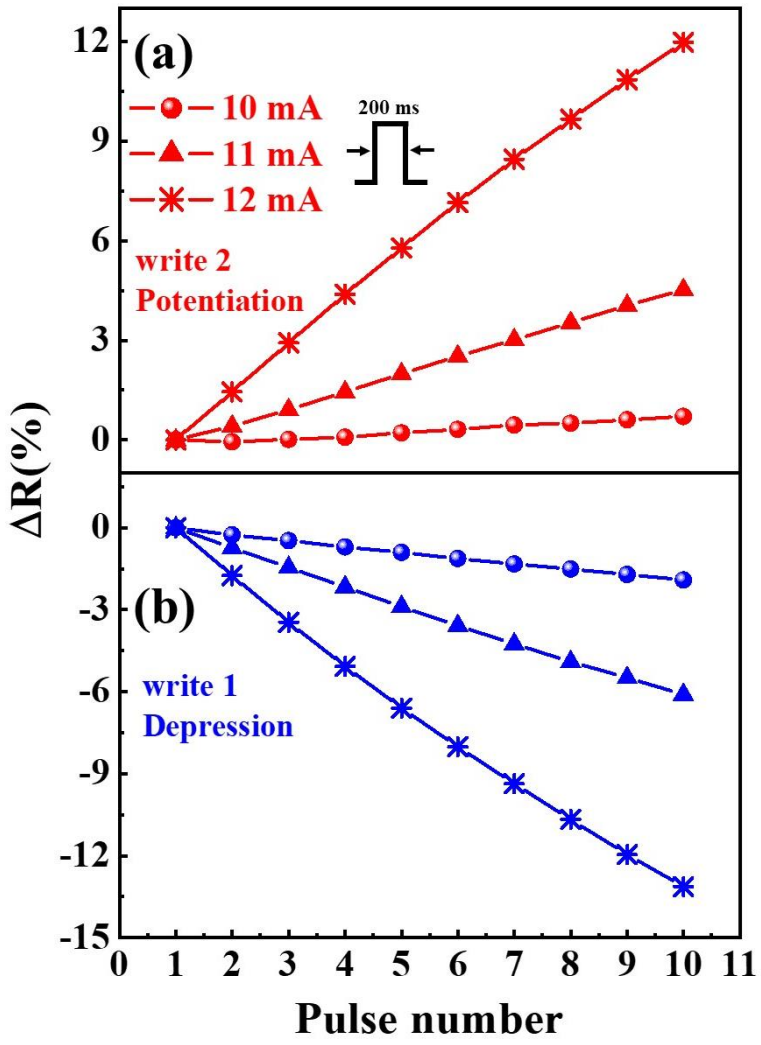

Figure 4-3: Current amplitude dependent writing process through (a) write 2 denoted as potentiation and (b) write 1 path denoted as depression.

In this writing process, the R_{xy} increases linearly and the variation becomes larger with higher writing current. It indicated that the higher writing pulse current produced more asymmetric temperature gradient and deflected more electrons. This behavior is denoted as potentiation corresponding to the increased synaptic weight. On the other hand, when we performed the writing process through write 1 path, the R_{xy}

doi:10.6342/NTU202301357

variated reversely [see Figure 4-3 (b)]. This behavior is denoted as depression, which corresponds to the decreased synaptic weight. The results shows that the synaptic weight (R_{xy}) can be variated arbitrarily by pulse current through different writing path. Additionally, to further examine the endurance of this device, we inject a pulse current train, which contains 10 consecutive pulses, each 14 mA in amplitude and 200 milliseconds in width, along the write 2 current path. As shown in Figure 4-4 (b), R_{xy} also increases linearly with the pulse current train. After multiple times of potentiation (60, 80, 120, 200), we inject the pulse train into the "write 1" current path (90° to the write 2 current path) and then read the R_{xy}. Conversely, it decreases linearly with the pulse current train. It is worthy to note that the change in synaptic weight is almost no limit (200 pulse trains) before the device breakdown, indicating that this device has very high endurance. Moreover, the potentiation and depression are still linear, nearly symmetric, and highly stable, which are critical for neuromorphic devices for high-accuracy computation [3]. If the variation of synaptic weight is not linear or not symmetric, the hardware usually needs additional and complicated operations to compensate for the non-idealities [3].

doi:10.6342/NTU202301357

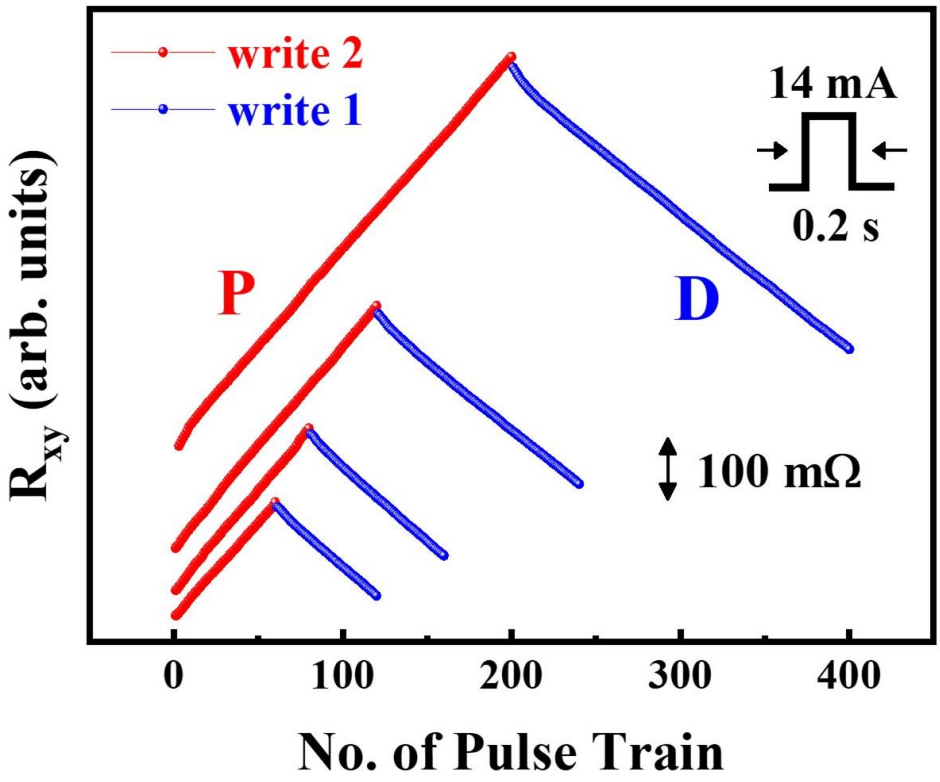

Figure 4-4: Realization of the potentiation (red) and depression (blue) with a writing current pulse of 14 mA injecting through write 2 and write 1 path, respectively. A reading probing current is 1 mA.

4.1.3 Property variation

In the previous work of AFM switching in single layer eight-terminal devices, the destruction of device due to the high writing current density [28]. This destruction of device causes the non-volatile change in transverse resistance. The non-volatile variation is not consistent with biological system and the destruction is bad for future application. Therefore, in this work, we separate the writing and reading layer by insulating SiO_2 layer to prevent structural destruction in reading layer (Bi) during the

doi:10.6342/NTU202301357

writing process. We first performed five consecutive writing processes containing both potentiation and depression with 13 mA and 400 ms writing pulse current. The comparison of the first and the fifth potentiation is presented in Figure 4-5 (a). the variation of synaptic weight has nearly the same behavior in the first and fifth writing process which contains 10 single pulse writing (13 mA with 400 ms width) process. The initial state of the transverse resistance only has 0.003 Ω difference, indicating the stability and small variation of device during the writing process. We estimate the variation between the two potentiation is about 0.02%, indicating the high stability and small variation of the device during the writing process. Furthermore, we have observed minimal property variation among devices in the same batch. This is demonstrated in Figure 4-5 (b), where the hall resistance between devices 12 and 4 only differs by approximately 2%. Moreover, the change in resistance ratio per 10-pulse potentiation process is less than 0.1%. It is also worthy to note that Bi has high Seebeck coefficient and relative low resistance compared with the reported memristors which is in the range of KΩ to MΩ [39]. It provides more resistance variation and reduces the power consumption in this device.

doi:10.6342/NTU202301357

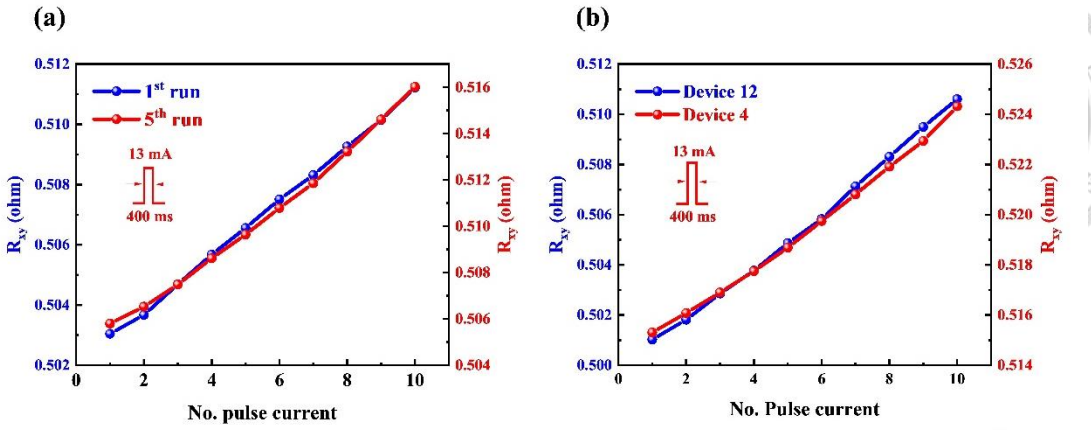

Figure 4-5: Property variation. Comparison of the synaptic weight variation in (a) first (blue) potentiation process and fifth (red) potentiation process in the same device and (b) in device 12 and device 4 during the same potentiation.

4.1.4 Anti-symmetric STDP

As mentioned in section 2.3.1, STDP is the key learning mechanism in biological system. The synapse variates its synaptic weight based on the delayed time between post- and pre-synaptic pulses [5,40]. Different types of STDP reflect their different functionalities in human brains. A synapse is composed of a post-synaptic dendrite, a pre-synaptic axon, and a cleft between the post- and pre-synapse. Transferring information is done by forward propagating a spike from a dendrite of the pre-synapse neuron through the synapse toward the axon of the post-synapse neuron. The biological synapses reconfigure their synaptic weights based on the timing and/or the sequence of spikes between pre- and post- synaptic neurons. In the human memory center (hippocampus), if the pre-synaptic neuron spike precedes the post-synaptic neuron

doi:10.6342/NTU202301357

spike ($\Delta t_{post\text{-}pre} > 0$), which follows the causality, the synaptic weight increases. On the contrary, if the order of the spike is opposite ($\Delta t_{post\text{-}pre} < 0$), the synaptic weight decreases since the events violate the causality. The synaptic weight on the $\Delta t_{post\text{-}pre}$ based on this behavior is anti-symmetric. In the artificial synapse, it is necessary that the STDP can be electronically emulated by combination of external stimulation. In this section, we successfully realize the anti-symmetric STDP by transferring the pulse width information into delayed timing information. First, we demonstrate the flexible control of the synaptic weight by the width of the writing current pulse. In Figure 4-6, we injected writing current pulses with different pulse widths along “write 1” and “write 2” paths to variate the synaptic weight. The weight of the synapse, both for the synaptic potentiation and depression, is proportional to the width of the pulses. The wider the pulse we injected into our device, the larger the ratio at which R_{xy} variated. The flexibility of operation in this device presents us with a greater range of possibilities to explore its applications.

doi:10.6342/NTU202301357

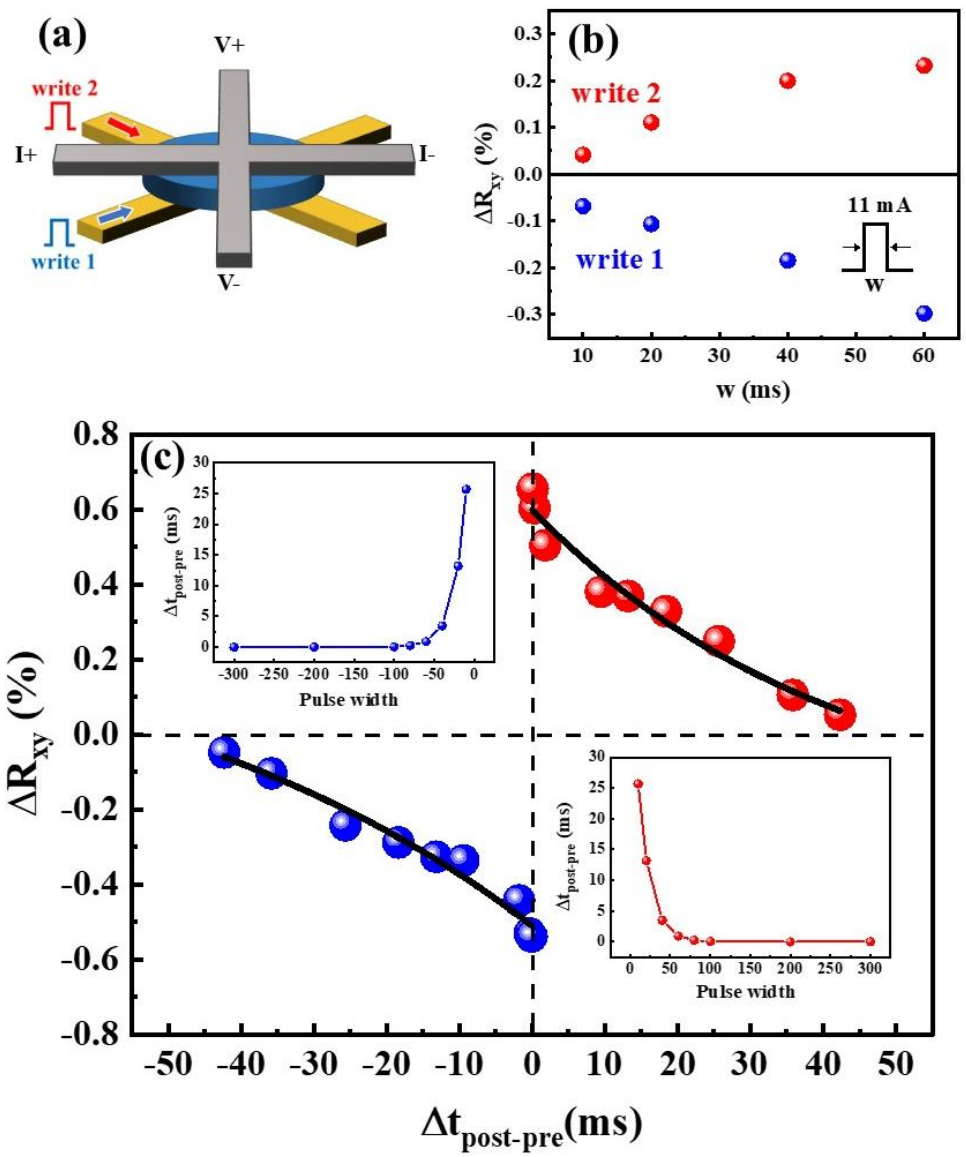

Figure 4-6: Anti-symmetric STDP. (a) Schematic diagram of pulse width dependent synaptic operation. (b) Pulse width dependent variation of synaptic weight. (c) Realization of anti-symmetric STDP. The inserts show the conversion between pulse width and relative timing information.

To emulate these STDPs electronically, we need dedicated programmed sequences of the writing current. In realizing anti-symmetric STDP, we convert the writing current pulse width (Δw_{pulse}) to the relative timing ($\Delta t_{post\text{-}pre}$) between the pre- and post- synaptic

doi:10.6342/NTU202301357

spikes. The converting equation is that $\Delta w_{pulse} = Ce^{\Delta t_{post-pre}/t_0}$, where $C = 0.05$ and $t_0 = 15$ms as presented in the inserts in Figure 4-6 (c). The C and t_0 are both constant which are chosen so that $\Delta t_{post-pre}$ is in the power of millisecond. Figure 4-6 (c) shows the realized anti-symmetric STDP, the synaptic weight R_{xy} increases when $\Delta t_{post-pre} > 0$ and decreases when $\Delta t_{post-pre} < 0$. The ΔR_{xy} reaches maximal value when $\Delta t_{post-pre}$ is close to zero and decays exponentially as $\Delta t_{post-pre}$ becomes larger (see the fitted curve). The relation between ΔR_{xy} and $\Delta t_{post-pre}$ is fit by an exponential function $\Delta R_{xy} = A e^{-\Delta t_{post-pre}/\tau}$, where the constant of proportionality A and time τ are estimated to be 0.847 % and 42.3 ms for $\Delta t_{post-pre} > 0$ and 0.876 % and 58.7 ms for $\Delta t_{post-pre} < 0$. The estimated values of τ are close to the observed value in the hippocampal neurons of rats [41]. This behavior emulates the synaptic weight change for an event that follows causality, representing biological behavior for hippocampal neurons [5,22].

4.1.5 Symmetric STDP

Besides anti-symmetric STDP, in some parts of the human brain, the STDP depends only on the timing of spikes but not in order; therefore, the synaptic weight on the $\Delta t_{post-pre}$ is symmetric. For example, the recurrent synapses between CA3 cells in the hippocampus variate their weight symmetrically (independent of the order of spikes)

doi:10.6342/NTU202301357

[22,42]. This specific STDP rule facilitates information storage and recall and enhances the reliability of pattern completion and storage capacity. Furthermore, studies have shown that symmetric STDP is more robust than anti-symmetric STDP in auto-associative neural networks [42].

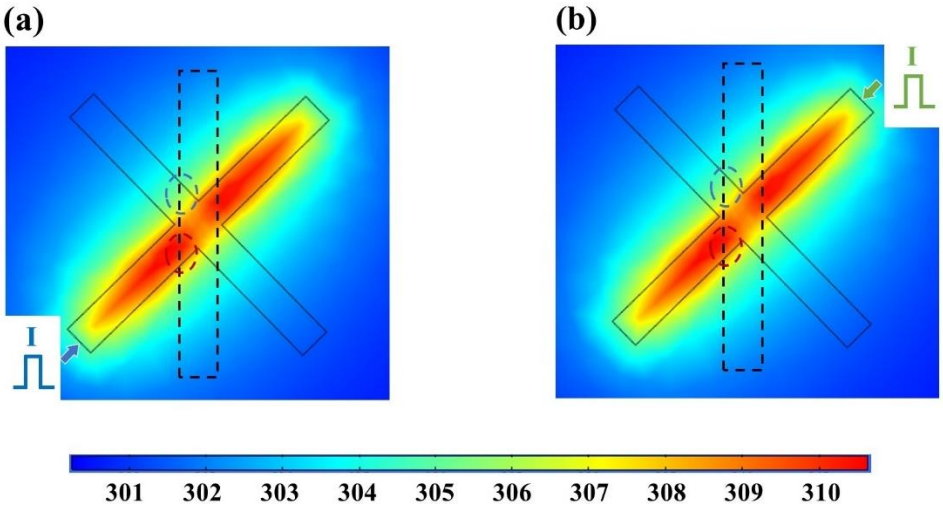

Figure 4-7: COMSOL simulation of temperature distribution after injecting a writing pulse current through (a) write 1 and (b) write 3 path.

We further successfully demonstrate the symmetric STDP behavior in the same multi-layer-multi-terminal heterostructures. Instead of injecting current from two paths with a 90° difference to implement the anti-symmetric STDP, we inject current from two paths with a 180° difference to realize symmetric STDP. Since the device structure is symmetric, the generated asymmetric temperature gradient is independent of the direction of writing current. The COMSOL simulations of temperature distribution for

doi:10.6342/NTU202301357

writing current injected through 45° (write 1) and 225° (write 3) are presented in Figure 4-7. Thus, the same polarity of temperature distribution is created when we inject a writing pulse current along the "write 3" terminal, which equals injecting a negative pulse current along the "write 1" terminal. Therefore, in the realization of symmetric STDP, we inject two separated writing pulse currents through "write 1" and "write 3", respectively, with delayed time $\Delta t_{post\text{-}pre}$ as sketched in Figure 4-8 (a). After the writing process, we measure the R_{xy} immediately and obtain the ΔR_{xy} (%). Figure 4-8 (b) shows the relation of ΔR_{xy} and delayed time, the variance of synaptic weight now depends only on $|\Delta t_{post-pre}|$, not on the order of spikes. When $|\Delta t_{post-pre}|$ is small, the synaptic weight increases dramatically but barely changes when $|\Delta t_{post-pre}|$ is large. Thus, we demonstrate both anti-symmetric and symmetric STDP in the same device using different terminals. As mentioned, different STDP rules represent different functionalities in the neural system and have varying impacts on neural information processing. Moreover, with the writing current flowing through different writing terminals, we are able to implement a hybrid model with both anti-symmetric and symmetric STDP learning rules, which provides a more stable and reliable design for neural networks. Our device, which realizes both anti-symmetric and symmetric STDP, offers a wealth of possibilities for exploring potential future applications in neuromorphic computing.

doi:10.6342/NTU202301357

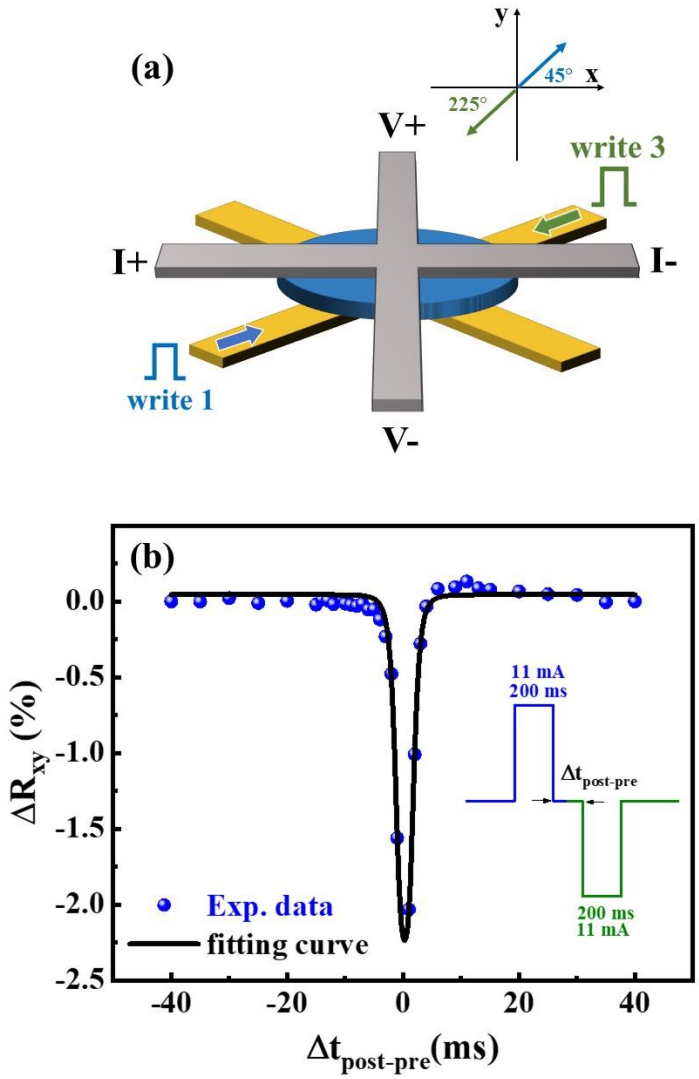

Figure 4-8: (a) Schematic diagram of operation of symmetric STDP. (b) Realized symmetric STDP.

4.1.6 Short-term plasticity

In the human brain, synaptic plasticity can be generally categorized into two types: long-term plasticity (LTP) and short-term plasticity (STP). The main difference between them is the time scale of retention of their synaptic weight. Generally, the

doi:10.6342/NTU202301357

synaptic modification that lasts for a long time (hours to days) after stimulation can be viewed as LTP [3]. On the other hand, the STP usually lasts for a few seconds to minutes, and the synaptic weight fades away back to the initial value. STP is critical for spatiotemporal information processing in biological systems [3,43]. To evaluate the behavior of retention of the synaptic weight in our device, we injected 10 consecutive writing current pulses along the "write 2" path before reading the R_{xy} continuously, as illustrated in the insert in Figure 4-9. After the potentiation of 10 consecutive pulses, R_{xy} decays exponentially to the initial state in a short time scale as shown in Figure 4-9. The decayed R_{xy} is fit with exponential function $R_{xy} = R_0 + Ae^{-t/\tau}$, where R_0 = -0.298 ($\pm$ 0.004), A = 0.0047 ($\pm$ 0.0002), and τ = 9.2 s ($\pm$ 0.8 s), which indicates the STP for our device. The nature of heat dissipation causes the short time constant after the potentiation/depression. Our devices imitate the synaptic properties of the human brain showing volatile properties. If we want to make nonvolatile devices, we can use spintronics-based devices with multi-magnetic domain walls to store information on states in each domain.

doi:10.6342/NTU202301357

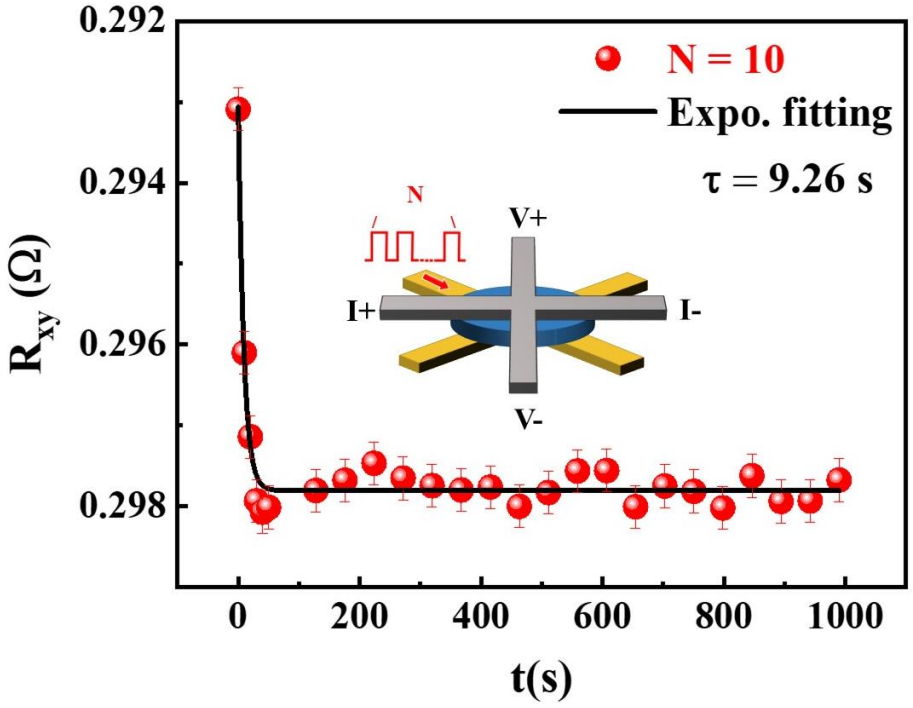

Figure 4-9: Forgetting or relaxation behavior after 10 consecutive writing processes. The inserted cartoon diagram shows the measurement sequences of the forgetting behavior. After N=10 writing current pulses, we read the R_{xy} continuously. The black line represents the exponential fitting curve with a time constant of 9.26 seconds.

doi:10.6342/NTU202301357

Chapter 5 AFM switching in Cr_2O_3

5.1 Cr_2O_3 (0001) thin film growth and structure characterization

The epitaxial Cr_2O_3 thin film is grown on the Al_2O_3 substrate. Since the crystal structure of Al_2O_3 substrate and Cr_2O_3 are both hexagonal, the epitaxial thin film can be deposited along the structure of substrate. Moreover, we can control the orientation of epitaxial thin film by choosing different orientation of Al_2O_3 substrate. There are three available orientation of Al_2O_3 substrate, including $(11\bar{2}0)$, $(10\bar{1}0)$, and (0001) as presented in Figure 5-1.

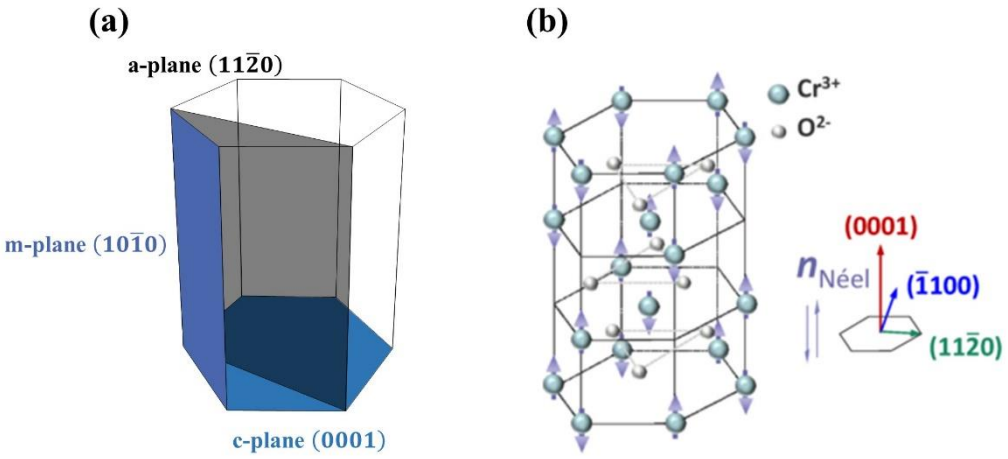

Figure 5-1: Crystal structure of Cr_2O_3. There are three available orientation of Al_2O_3 substrate $(11\bar{2}0)$, $(10\bar{1}0)$, and (0001). The Néel vector is along the (0001) direction.

doi:10.6342/NTU202301357

In detail, we use magnetron sputtering to deposit Cr on the Al_2O_3 substrate in O_2 environment under high temperature. For (0001)-oriented thin film, we deposit Cr at 500°C with 4 mTorr of mixed gas of O_2 and Ar for 2 hours on (0001)-oriented Al_2O_3 substrate. Then, the thin film structure is characterized by XRD as shown in Figure 5-2. The peak of Cr_2O_3 was sharp and close to the peak of Al_2O_3 substrate, indicating that thin film structure was along with the substrate. To further characterize the quality of Cr_2O_3 thin film, we perform the rocking curve measurement and do the fitting with Lorentz function to calculate the full width at half maximum (FWHM) as shown in Figure 5-2 (b). The calculated FWHM is 0.069° which indicating the high crystal quality of Cr_2O_3 (0001)-oriented thin film.

doi:10.6342/NTU202301357

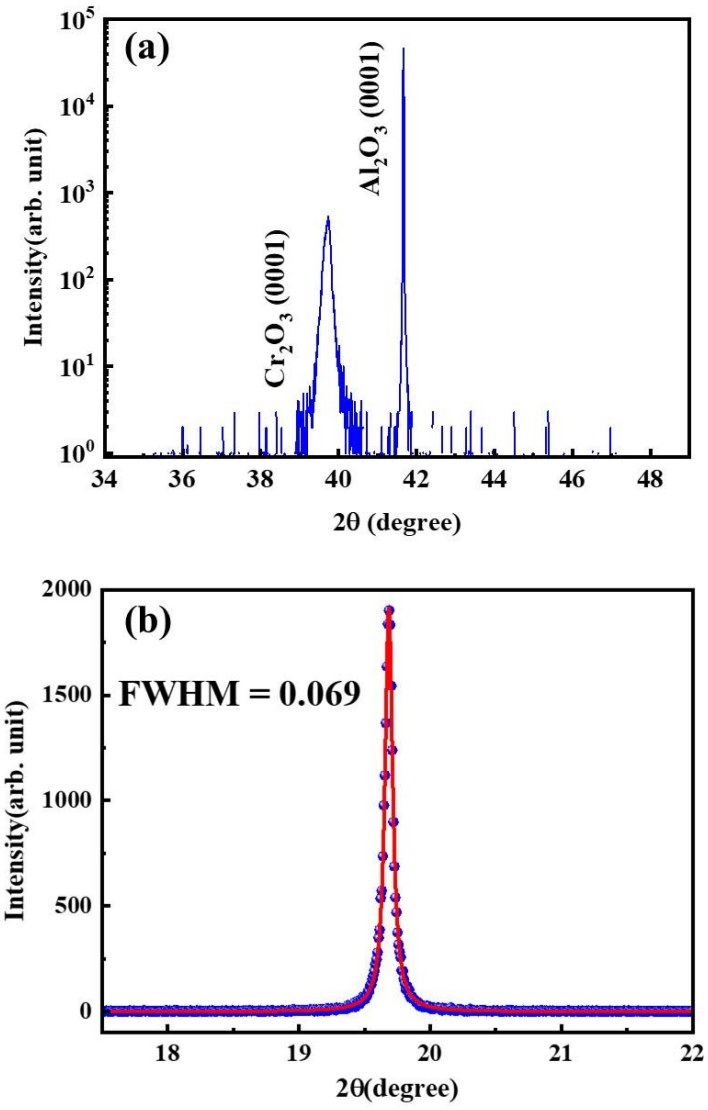

Figure 5-2: (a) XRD spectrum of Cr_2O_3 (0001)k(11 $\bar{2}$ 0). (b) Rocking curve measurement of Cr_2O_3 (0001)k(11$\bar{2}$0).

doi:10.6342/NTU202301357

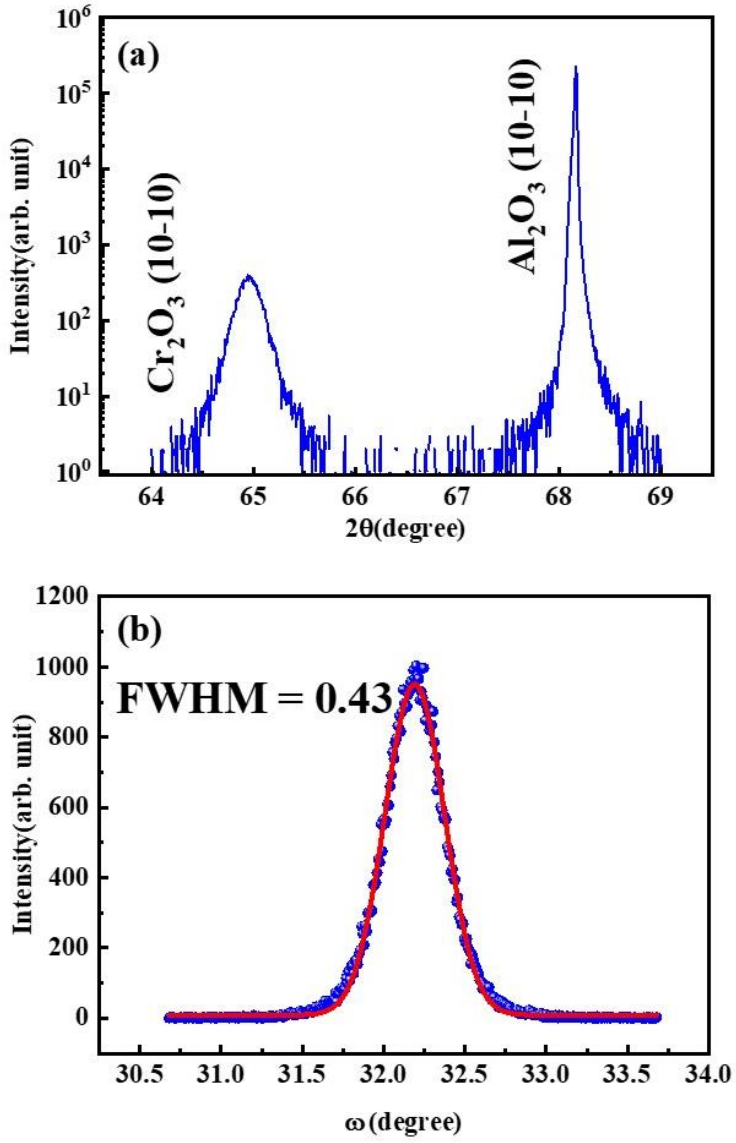

Figure 5-3: (a) XRD spectrum of Cr_2O_3 (10 $\bar{1}$ 0)k(0001). (b) Rocking curve measurement of Cr_2O_3 (10$\bar{1}$0)k(0001).

Even though the thin film quality of (10$\bar{1}$0)-oriented Cr_2O_3 is not good enough, the (0001)-oriented thin film has good quality. Therefore, we tried to do the electrical measurement (both transverse and longitudinal) to detect the spin-flop transition. In detail, we grew 5 nm Pt layer on the (0001)-oriented thin film and use the etching process to fabricate the Hall-bar. Then, we use PPMS to perform the electrical

doi:10.6342/NTU202301357

measurement (both transverse and longitudinal) on device B32 under magnetic field at 2 K as shown in Figure 5-4. However, there is no obvious spin-flop transition under high magnetic field up to 7 T. We think that the fluctuated signal in longitudinal measurement is due to the poor interface between Cr_2O_3 and Pt since we do not grow the Pt layer in-situ. Therefore, we tried to grow the Pt detection layer in-situ after growing single crystal Cr_2O_3 thin film. On the other hand, due to the lattice mismatch between Al_2O_3 substrate and Cr_2O_3, it might strongly subpress the Néel temperature [44]. It might be the reason do not observe the spin-flop transition at 5.8 T as bulk is. Therefore, we tried to grow a Pt buffer on the Al_2O_3 substrate first to improve the lattice matching in next section [44].

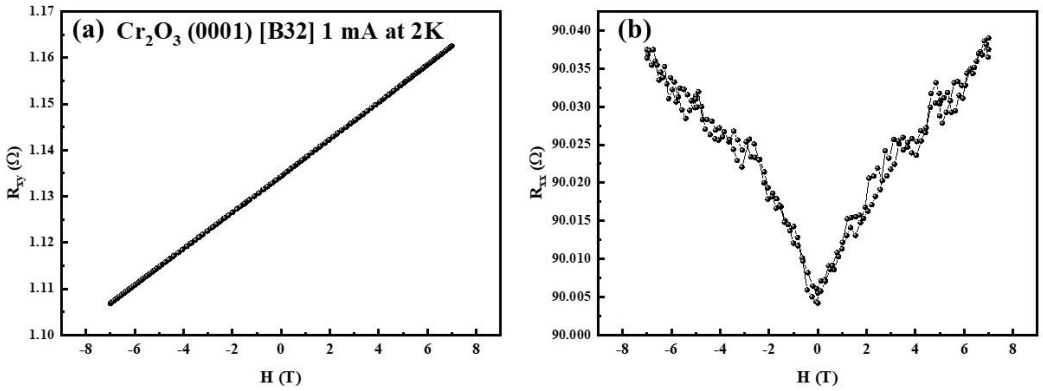

Figure 5-4: Electrical measurement under magnetic field in Cr_2O_3 at 2K. (a) Hall measurement on Pt. (b) Longitudinal measurement on Pt.

5.2 Pt/Cr_2O_3/Pt tri-layer

We tried to grow a Pt buffet layer with 20 nm thickness under 500°C on the Al_2O_3 substrate first to improve the lattice matching between Al_2O_3 substrate and C_2O_3 thin

doi:10.6342/NTU202301357

film. Additionally, after cooling down to room temperature, we grew 5 nm Pt detection layer on C_2O_3 in-situ. Under high temperature, Pt prefer to form (111) direction whose lattice constant is between Al_2O_3 and C_2O_3. The XRD characterization of tri-layer is presented in Figure 5-5. The diffraction signal of C_2O_3 thin film is much larger than previous one. Moreover, we can observe the Laue diffraction (oscillation in XRD pattern) which only exists in high quality single crystal thin film. The rocking curve measurement also reveals the same result, the 0.053° is narrower than the previous one, indicating the higher quality.

doi:10.6342/NTU202301357

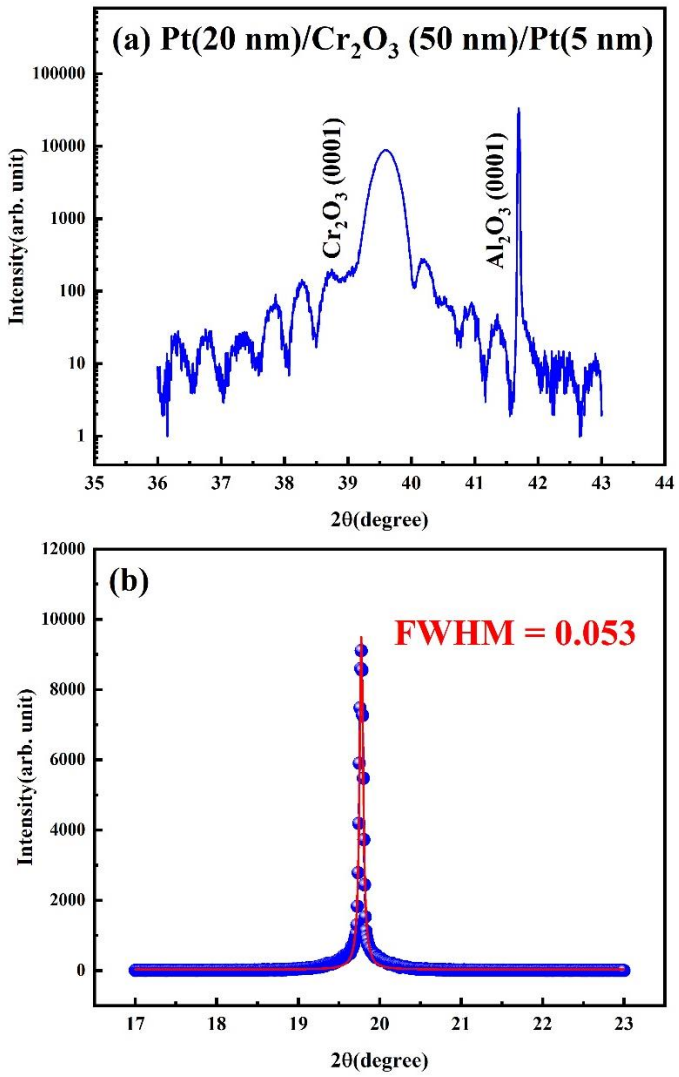

Figure 5-5: (a) XRD spectrum of tri-layer Pt/Cr_2O_3 (0001)k(11$\bar{2}$0)/Pt. (b) Rocking curve measurement of tri-layer Pt/Cr_2O_3 (0001)k(11$\bar{2}$0)/Pt.

Then, we fabricate the Pt detection layer into Hall bar by etching process and perform the electrical measurement on device B35 at 2K as shown in Figure 5-6. However, the spin-flop transition is still not be observed even we improve the lattice matching. But we do observe the stable signal in longitudinal measurement after we improve the interface. Moreover, we observe the anomalous Hall effect in the interface Cr_2O_3/Pt which is due to the proximity effect in the interface between AFM insulator and heavy

doi:10.6342/NTU202301357

metal [45-47]. Additionally, we further perform the temperature dependent anomalous Hall measurements on the same device as shown in Figure 5-7. The AHE on device B35 decreases as temperature increasing.

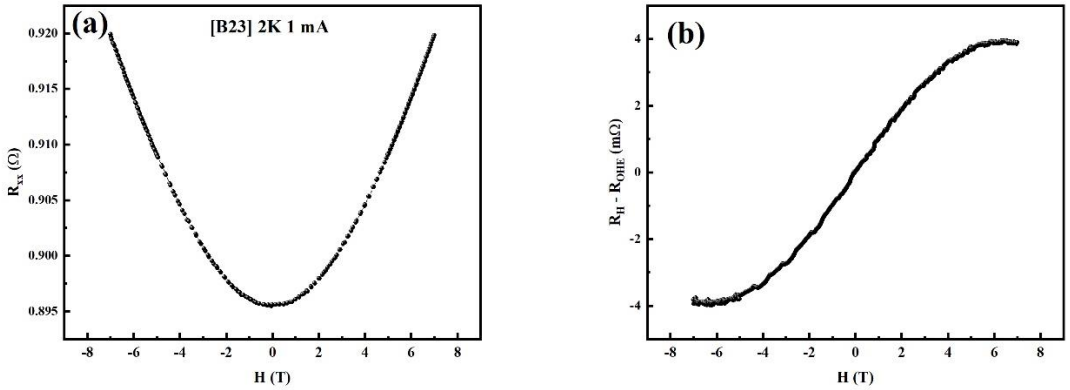

Figure 5-6: Electrical measurement under magnetic field in tri-layer Pt/Cr_2O_3/Pt presented in Figure 5.5 at 2K. (a) Longitudinal on Pt. (b) Hall measurement on Pt which substrate the background of ordinary Hall effect.

doi:10.6342/NTU202301357

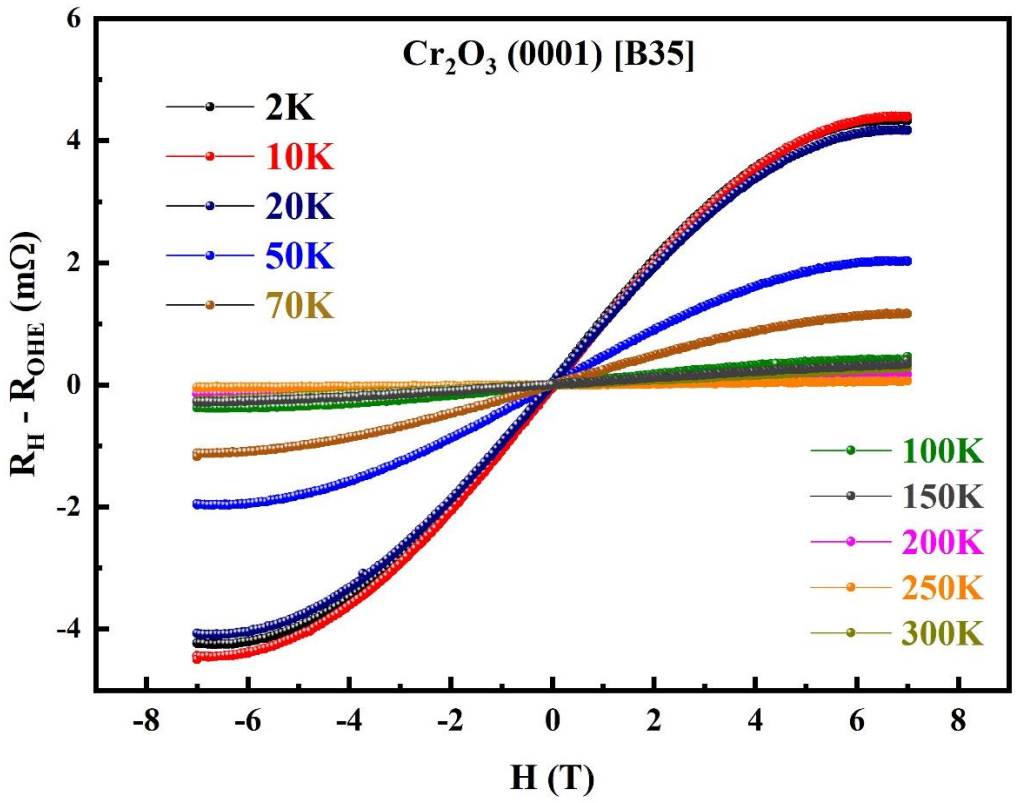

Figure 5-7: Anomalous Hall measurement under different temperature on the device B35.

We then extract the anomalous Hall resistance as shown in Figure 5-8, the anomalous Hall resistance decrease as temperature increasing and disappears within 200~250K. Therefore, this indicates that the Néel temperature of Cr2O3 is within thin region. This proximity effect induced anomalous Hall effect is related to the antiferromagnetism of Cr_2O_3 [44]. By doing so, we can indirectly detect the Néel temperature by electrical measurement.

doi:10.6342/NTU202301357

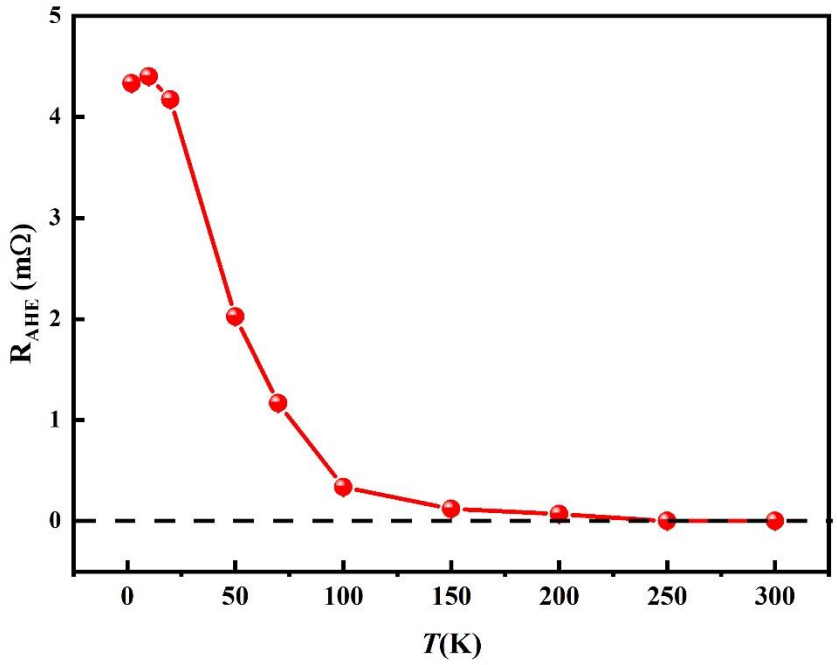

Figure 5-8: Temperature dependent anomalous Hall resistance extracted from figure 5-7. The dot line indicates the disappearance of anomalous Hall effect.

Although we still not observe the spin-flop transition under magnetic field up to 7T, we believe it is on the right path. In our future work, we try to variate the thickness of Pt buffer layer or the thickness of Cr_2O_3, trying to electrically detect the spin-flop transition.

doi:10.6342/NTU202301357

Chapter 6 Conclusion

This work introduces a multi-layer, multi-terminal neuromorphic computing device that emulates the synaptic plasticity by the current-induced asymmetric heating accumulation. The writing and reading layers are separated by an insulating layer, enabling multiple synaptic functionalities and high-endurance operations. We use a pulse current to create the asymmetric temperature gradient in this device and immediately measure the transverse resistance from a reading current. We demonstrate various synaptic functions utilizing a sequence of writing current pulses, including linear potentiation and depression. Moreover, we realize both anti-symmetric and symmetric STDP based on writing current paths, pulse widths, and relative timing in the same device. The device has a simple structure and operational process, leading to robust thermal-driven electrical signals that can be easily tailored to meet specific requirements through adjustments to the materials' Seebeck coefficient. With high linearity, reliability, and multiple functionalities, this thermal-driven multi-terminal device offers an energy-efficient platform for future neuromorphic computing devices in artificial intelligence applications.

As for the AFM C_2O_3 part, we successfully grow high-quality (0001) epitaxial thin film on (0001) Al_2O_3 substrate by the help of Pt buffer layer. Moreover, we observed the anomalous Hall effect in the interface of Pt/Cr_2O_3 which is believed to be induced

doi:10.6342/NTU202301357

by proximity effect. Thus, we are able to use the anomalous Hall effect to detect the antiferromagnetism in Cr_2O_3. This technique provides us a platform to electrically detect the Néel temperature in antiferromagnetic materials. However, we still cannot observe the spin-flop transition on electrical transport measurement. We think that is due to the magnetoelastic effect from the mismatch between Cr_2O_3 and Al_2O_3 substrate. In the future, we suggest growing a Pt buffer layer to improve the lattice match and detect the spin-flop transition electrically.

Reference

[1] NEUMANN, J. v. The Principles of Large-Scale Computing Machines. *Annals of the History of Computing* **10**, 243-256 (1988).

[2] Backus, J. Can Programming Be Liberated from Von Neumann Style - Functional Style and Its Algebra of Programs. *Commun Acm* **21**, 613-641 (1978).

[3] Zhu, J. D., Zhang, T., Yang, Y. C. & Huang, R. A comprehensive review on emerging artificial neuromorphic devices. *Appl Phys Rev* **7**, 011312 (2020).

[4] Jo, S. H. *et al.* Nanoscale Memristor Device as Synapse in Neuromorphic Systems. *Nano Lett* **10**, 1297-1301 (2010).

[5] Bi, G.-q. & Poo, M.-m. Synaptic Modifications in Cultured Hippocampal Neurons: Dependence on Spike Timing, Synaptic Strength, and Postsynaptic Cell Type. *The Journal of Neuroscience* **18**, 10464 (1998).

[6] Xu, M. *et al.* Recent Advances on Neuromorphic Devices Based on Chalcogenide Phase-Change Materials. *Adv Funct Mater* **30**, 2003419 (2020).

[7] Wadley, P. *et al.* Electrical switching of an antiferromagnet. *Science* **351**, 587-590 (2016).

[8] Chen, X. Z. *et al.* Antidamping-Torque-Induced Switching in Biaxial Antiferromagnetic Insulators. *Phys Rev Lett* **120** (2018).

[9] Chiang, C. C., Huang, S. Y., Qu, D., Wu, P. H. & Chien, C. L. Absence of Evidence of Electrical Switching of the Antiferromagnetic Neel Vector. *Phys*

doi:10.6342/NTU202301357

Rev Lett **123**, 227203 (2019).

[10] Zhang, Y. H., Chuang, T. C., Qu, D. R. & Huang, S. Y. Detection and manipulation of the antiferromagnetic Neel vector in Cr2O3. *Phys Rev B* **105** (2022).

[11] Kurenkov, A., Fukami, S. & Ohno, H. Neuromorphic computing with antiferromagnetic spintronics. *J Appl Phys* **128**, 010902 (2020).

[12] Huang, Y. H. *et al.* A Spin-Orbit Torque Ratchet at Ferromagnet/Antiferromagnet Interface via Exchange Spring. *Adv Funct Mater* **32**, 2111653 (2022).

[13] Pai, C.-F. & Tang, D. D. *MAGNETIC MEMORY TECHNOLOGY: Spin-transfer-torque Mram and Beyond*. (John Wiley & Sons, 2020).

[14] Coey, J. M. *Magnetism and magnetic materials*. (Cambridge university press, 2010).

[15] Cullity, B. D. & Graham, C. D. *Introduction to magnetic materials*. (John Wiley & Sons, 2011).

[16] Hirsch, J. E. Spin Hall effect. *Phys Rev Lett* **83**, 1834-1837 (1999).

[17] Sinova, J., Valenzuela, S. O., Wunderlich, J., Back, C. H. & Jungwirth, T. Spin Hall effects. *Rev Mod Phys* **87**, 1213-1259 (2015).

[18] Hoffmann, A. Spin Hall Effects in Metals. *Ieee T Magn* **49**, 5172-5193 (2013).

[19] Dyakonov, M. I. & Perel, V. Current-induced spin orientation of electrons in semiconductors. *Physics Letters A* **35**, 459-460 (1971).

[20] Dyakonov, M. I. & Perel, V. I. Possibility of Orienting Electron Spins with Current. *Jetp Lett-Ussr* **13**, 467-& (1971).

[21] Markram, H., Gerstner, W. & Sjöström, P. J. Spike-Timing-Dependent Plasticity: A Comprehensive Overview. *Frontiers in Synaptic Neuroscience* **4**, 00002 (2012).

[22] Abbott, L. F. & Nelson, S. B. Synaptic plasticity: taming the beast. *Nat Neurosci* **3**, 1178-1183 (2000).

[23] Tang, D. D., Wang, P. K., Speriosu, V. S., Le, S. & Kung, K. K. Spin-Valve Ram Cell. *Ieee T Magn* **31**, 3206-3208 (1995).

[24] Tang, D. D. & Lee, Y.-J. *Magnetic memory: fundamentals and technology*. (Cambridge University Press, 2010).

[25] Fukami, S., Anekawa, T., Zhang, C. & Ohno, H. A spin-orbit torque switching scheme with collinear magnetic easy axis and current configuration. *Nat Nanotechnol* **11**, 621-+ (2016).

[26] Wang, Y. H. *et al.* in *2012 International Electron Devices Meeting.* 29.22.21-29.22.24.

[27] Zelezny, J. *et al.* Relativistic Neel-Order Fields Induced by Electrical Current

doi:10.6342/NTU202301357

in Antiferromagnets. *Phys Rev Lett* **113** (2014).

[28] Churikova, A. *et al.* Non-magnetic origin of spin Hall magnetoresistance-like signals in Pt films and epitaxial NiO/Pt bilayers. *Appl Phys Lett* **116**, 022410 (2020).

[29] Hu, S. *et al.* Current-Induced Planar Resistive Switching Mediated by Oxygen Migration in NiO/Pt Bilayer. *Adv Electron Mater* **6** (2020).

[30] Jacot, B. J. *et al.* Systematic study of nonmagnetic resistance changes due to electrical pulsing in single metal layers and metal/antiferromagnet bilayers. *J Appl Phys* **128** (2020).

[31] Matalla-Wagner, T., Schmalhorst, J. M., Reiss, G., Tamura, N. & Meinert, M. Resistive contribution in electrical-switching experiments with antiferromagnets. *Phys Rev Res* **2**, 033077 (2020).

[32] Sheng, P., Zhao, Z. Y., Benally, O. J., Zhang, D. L. & Wang, J. P. Thermal contribution in the electrical switching experiments with heavy metal/antiferromagnet structures. *J Appl Phys* **132** (2022).

[33] Foner, S. High-Field Antiferromagnetic Resonance in ${\mathrm{Cr}}_{2}$${\mathrm{O}}_{3}$. *Physical Review* **130**, 183-197 (1963).

[34] Binnig, G., Quate, C. F. & Gerber, C. Atomic Force Microscope. *Phys Rev Lett* **56**, 930-933 (1986).

[35] Chen, H. J., Chiang, C. C., Cheng, C. Y., Qu, D. & Huang, S. Y. Neuromorphic computing devices based on the asymmetric temperature gradient. *Appl Phys Lett* **122** (2023).

[36] Moffat, R. J. Notes on using thermocouples. *Electronics Cooling* **3**, 12-15 (1997).

[37] Mishra, R., Kumar, D. & Yang, H. Oxygen-Migration-Based Spintronic Device Emulating a Biological Synapse. *Phys Rev Appl* **11**, 054065 (2019).

[38] Cheng, Y., Yu, S. S., Zhu, M. L., Hwang, J. & Yang, F. Y. Electrical Switching of Tristate Antiferromagnetic Neel Order in alpha-Fe2O3 Epitaxial Films. *Phys Rev Lett* **124**, 027202 (2020).

[39] Li, Y. B., Wang, Z. R., Midya, R., Xia, Q. F. & Yang, J. J. Review of memristor devices in neuromorphic computing: materials sciences and device challenges. *J Phys D Appl Phys* **51**, 503002 (2018).

[40] Wang, H. X., Gerkin, R. C., Nauen, D. W. & Bi, G. Q. Coactivation and timing-dependent integration of synaptic potentiation and depression. *Nat Neurosci* **8**, 187-193 (2005).

[41] Bi, G.-q. & Poo, M.-m. Synaptic modification by correlated activity: Hebb's postulate revisited. *Annu Rev Neurosci* **24**, 139-166 (2001).

doi:10.6342/NTU202301357

[42] Mishra, R. K., Kim, S., Guzman, S. J. & Jonas, P. Symmetric spike timing-dependent plasticity at CA3-CA3 synapses optimizes storage and recall in autoassociative networks. *Nat Commun* **7**, 11552 (2016).

[43] Abbott, L. F. & Regehr, W. G. Synaptic computation. *Nature* **431**, 796-803 (2004).

[44] Wang, X. R., Ujimoto, K., Toyoki, K., Nakatani, R. & Shiratsuchi, Y. Increase of Neel temperature of magnetoelectric Cr2O3 thin film by epitaxial lattice matching. *Appl Phys Lett* **121**, 182402 (2022).

[45] Ruegg, S. *et al.* Spin-Dependent X-Ray Absorption in Co/Pt Multilayers. *J Appl Phys* **69**, 5655-5657 (1991).

[46] Schutz, G. *et al.* Distribution of Magnetic-Moments in Co/Pt and Co/Pt/Ir/Pt Multilayers Detected by Magnetic-X-Ray Absorption. *J Appl Phys* **73**, 6430-6432 (1993).

[47] Suzuki, M. *et al.* Depth profile of spin and orbital magnetic moments in a subnanometer Pt film on Co. *Phys Rev B* **72** (2005).

doi:10.6342/NTU202301357